



# Recent Advances in Rechargeable Magnesium-Based Batteries for High-Efficiency Energy Storage

Ziqi Guo, Shuoqing Zhao, Tiexin Li, Dawei Su,\* Shaojun Guo, and Guoxiu Wang\*

**Benefiting from higher volumetric capacity, environmental friendliness and metallic dendrite-free magnesium (Mg) anodes, rechargeable magnesium batteries (RMBs) are of great importance to the development of energy storage technology beyond lithium-ion batteries (LIBs). However, their practical applications are still limited by the absence of suitable electrode materials, the sluggish kinetics of Mg<sup>2+</sup> insertion/extraction and incompatibilities between electrodes and electrolytes. Herein, a systematic and insightful review of recent advances in RMBs, including intercalation-based cathode materials and conversion reaction-based compounds is presented. The relationship between microstructures with their electrochemical performances is comprehensively elucidated. In particular, anode materials are discussed beyond metallic Mg for RMBs. Furthermore, other Mg-based battery systems are also summarized, including Mg–air batteries, Mg–sulfur batteries, and Mg–iodine batteries. This review provides a comprehensive understanding of Mg-based energy storage technology and could offer new strategies for designing high-performance rechargeable magnesium batteries.**

## 1. Introduction

The burning of fossil fuels has caused severe environmental issues, including poor air quality and global warming. Therefore, low-cost and grid-scale energy storage for renewable energy is indispensable for sustainable development.<sup>[1,2]</sup> Most of renewable energy sources such as wind, solar, and tidal energy, are intermittent, depending on the weather conditions to generate electricity. Lithium-ion battery (LIB) is the state-of-the-art energy storage device for powering electric vehicles and portable electronics.<sup>[2–5]</sup> However, the current LIBs still cannot meet the ever-increasing requirement for high energy density and safety.<sup>[6–8]</sup> Moreover, their large-scale developments are still hindered by the uneven and limited distribution

of lithium resources in the earth's crust (0.0022 wt%).<sup>[9]</sup> Therefore, it is critical to develop new battery systems.<sup>[10]</sup>

Multivalent-ion batteries can in principle provide higher energy density than monovalent LIBs, which could overcome the aforementioned problems by employing a non-Li metallic anode.<sup>[11–13]</sup> Among various candidates, rechargeable magnesium batteries have many advantages over LIBs, such as abundant Mg resources, small ionic radius (0.72 Å) and high theoretical volumetric capacity (3833 mAh cm<sup>-3</sup>) (Figure 1a). Particularly, RMBs are inherently safer than LIBs because metallic Mg anodes are dendrite-free upon cycling.<sup>[14–17]</sup> In addition, Mg also possesses higher oxidative stability than lithium.<sup>[18]</sup>

The configurations and working mechanisms of RMBs are similar to those of LIBs (Figure 1b,c). However, the current research on RMBs still faces many challenges. Par-

ticularly, metallic Mg anodes have a strong tendency to form an insulated and passivating surface layer, which kinetically blocks electrochemical reactions at room temperature.<sup>[19–21]</sup> Such passivating layers engender difficulty for choosing compatible electrodes and electrolytes.<sup>[22,23]</sup> In addition, many RMBs electrolytes are air-sensitive, highly corrosive and flammable,<sup>[24,25]</sup> which poses a threat to their practical applications. Additionally, it is challenging to quest for suitable cathode materials with the rapid intercalation/deintercalation of Mg<sup>2+</sup> at room temperature, considering the complex reaction mechanism of Mg-based electrochemistry. Many useful pioneering works have been devoted to developing cathode materials for RMBs (Figure 1d).<sup>[26–28]</sup> The strong electrostatic interaction of Mg<sup>2+</sup> inevitably results in sluggish kinetics, which is kinetically slower than Li<sup>+</sup>, especially at room temperature.<sup>[19]</sup>

In this review, we summarize recently developed cathode materials for rechargeable magnesium-ion batteries. The anode materials beyond Mg metal are also discussed. Furthermore, we explored other Mg-based energy storage technologies, including Mg–air batteries, Mg–sulfur batteries, and Mg–iodine batteries. This review could also provide basic knowledge and valuable strategies for the advancement of high-energy-density rechargeable magnesium-based batteries.

## 2. Cathode Materials

Similar to LIBs, the working mechanism of RMBs batteries are based on the shuttle of Mg<sup>2+</sup> ions between cathode and anode

Z. Guo, S. Zhao, T. Li, Dr. D. Su, Prof. G. Wang  
Centre for Clean Energy Technology  
University of Technology Sydney  
Broadway, NSW 2007, Australia  
E-mail: dawei.su@uts.edu.au; guoxiu.wang@uts.edu.au  
Prof. S. Guo  
Department of Materials Science and Engineering  
College of Engineering  
Peking University  
Beijing 100871, China

The ORCID identification number(s) for the author(s) of this article can be found under <https://doi.org/10.1002/aenm.201903591>.

DOI: 10.1002/aenm.201903591

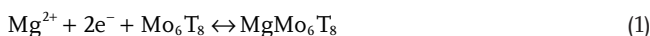
(Figure 1a). However,  $Mg^{2+}$  intercalation in solids is kinetically slower than  $Li^+$ , especially at room temperature. This phenomenon is mainly ascribed to the divalent nature of  $Mg^{2+}$ .<sup>[28,33]</sup> Another problem is the strong electrostatic interaction between the cathode host and  $Mg^{2+}$ , which inevitably leads to sluggish kinetics and results in poor rate performance.<sup>[34,35]</sup> Whereas, a metallic Mg anode is expected to undergo the two-electron charge transfers, which is superior to lithium metal anodes with only one-electron transfer. Therefore, a suitable RMB cathode, which can reversibly receive/release  $Mg^{2+}$  during electrochemical processes, is capable of delivering around double the discharge capacity of the current state-of-art LIBs cathodes.<sup>[18]</sup>

## 2.1. Intercalation Cathode Materials

Intercalation-type compounds are the most important and widely discussed cathode materials in RMBs systems. Owing to the great success of their counterparts in LIBs, these compounds are considered as the most promising candidates for RMBs. Previous findings have already confirmed that the diffusion behavior of multivalent cations usually depends on the crystal structure of cathode materials,<sup>[36]</sup> which determines the intercalation chemistry and ion mobility in these materials.<sup>[16,37,38]</sup> Therefore, the coordinating effect of diffusion networks facilitates the transport of multivalent cations and can cushion lattice expansion.<sup>[39,40]</sup> The intercalation cathode materials for typical RMBs can be classified according to the phase-structured materials.

### 2.1.1. Chevrel Phase Cathode Materials

The Chevrel phase ( $CP$ ,  $Mo_6T_8$ ;  $T = S$ ,  $Se$ ,  $Te$ ) is the first and the most successful intercalation cathode material for RMBs. This distinct category of host materials has been proven to effectively accommodate monovalent ( $Li^+$  and  $Na^+$ ) and multivalent ( $Zn^{2+}$ ,  $Mn^{2+}$ ,  $Ni^{2+}$ ,  $Co^{2+}$ , and  $Mg^{2+}$ ) cationic species.<sup>[27]</sup> A CP-based cathode not only shows energy storage capacity competitive with LIBs, but also serves as a standard to evaluate the electrochemical activity of newly developed magnesium electrolytes and membranes.<sup>[41–45]</sup> A typical CPs  $Mo_6T_8$  can maximum accommodate two  $Mg^{2+}$  ions per unit formula through charge exchange within the metallic  $Mo_6$  cluster as shown in Figure 2a.<sup>[14,19,27]</sup> Generally, the intercalation of  $Mg^{2+}$  into the CP host needs two steps<sup>[46–48]</sup>



These two-step processes with fast and efficient reaction kinetics at room temperature make CPs a promising cathode material for RMBs. The Chevrel phase  $Mo_6S_8$  has a unique crystal structure, in which  $S_8$  anions reside in the corners and octahedron  $Mo_6$  atoms occupy the faces of the cube (Figure 2a).<sup>[49]</sup> The displacement of highly symmetric 3a or 9d positions is favorable for  $Mg^{2+}$  diffusion (Figure 2b). Figure 2c exhibits two different hopping modes in  $Mo_6S_8$ . As



**Dawei Su** is Senior Lecturer for School of Mathematical and Physical Sciences in Faculty of Science. His original research related to advanced energy storage and conversion, including rechargeable lithium-ion, sodium-ion, potassium-ion, lithium-sulfur, and lithium-Air ( $O_2$ ) batteries. Especially, he is a pioneer in the study of sodium-ion batteries. His research activities involve the design, investigation and development of novel nanostructured materials for batteries applications.



**Guoxiu Wang** is the Director of the Centre for Clean Energy Technology and a Distinguished Professor at University of Technology Sydney (UTS), Australia. He is an expert in materials chemistry, electrochemistry, energy storage and conversion, and battery technologies. His research interests include lithium-ion batteries, lithium-air batteries, sodium-ion batteries, lithium-sulfur batteries, supercapacitors, hydrogen storage materials, fuel-cells, graphene, and chemical functionalization of graphene.

the inner-ring diffusion is much faster than the outer-ring diffusion, only the later facilitates the migration of  $Mg^{2+}$ . Hence, the presence of unoccupied sites among 12 sites per unit cell can provide solid-state diffusion channels and thus enhance the ionic conductivity of CPs (Figure 2d).<sup>[19]</sup> However, a major drawback of  $Mo_6S_8$  is the relatively low intercalation/deintercalation voltage ( $\approx 1.1$  V vs  $Mg^{2+}/Mg$ ), which will undoubtedly lower the output energy density of this RMBs system. Apart from this, it is impossible to completely extract all  $Mg^{2+}$  from CP  $Mo_6S_8$  at room temperature because of the presence of partial charge trapping within the material. A maximal discharge capacity ( $128.8$  mAh g<sup>-1</sup>) of  $Mo_6S_8$  cannot be achieved until the working temperature is higher than  $60$  °C. This phenomenon is due to the rapid  $Mg^{2+}$  diffusion kinetics at elevated temperatures in CPs.<sup>[19,50,51]</sup> Furthermore, Suresh et al.<sup>[52]</sup> reported an effect on partial chalcogen substitution in the  $Mo_6S_8$  CP ( $Mo_6Se_{8-n}S_n$ ) to modify the reversibility and mobility of  $Mg^{2+}$ . The intercalation/deintercalation mechanism of Chevrel phase was carefully investigated in the halide electrolyte.<sup>[45]</sup>  $Mg^{2+}$  ions coordinate with  $Cl^-$  and generate charged  $Mg_xCl_y^+$  species. The intercalation of  $Mg^{2+}$  causes the break of  $Mg-Cl$  ionic bond, therefore, resulting in  $Cl^-$  on the surface of Chevrel phase. These  $Cl^-$  species were associated with surface Mo and passivated the open

| Category   | Li     | Na    | K     | Mg    | Ca     | Zn     |
|--|--------|-------|-------|-------|--------|--------|
| Ionic radius ( $\text{\AA}$ )                            | 0.76   | 1.02  | 1.38  | 0.72  | 0.99   | 0.75   |
| Atomic mass ( $\text{g mol}^{-1}$ )                      | 6.94   | 22.99 | 39.10 | 24.30 | 40.07  | 65.38  |
| Voltage (vs. the SHE) (V)                                | -3.05  | -2.71 | -2.92 | -2.35 | -2.84  | -0.763 |
| Abundance in the earth's crust (wt%)                     | 0.0022 | 2.56  | 1.5   | 1.35  | 2.94   | 0.0078 |
| Capacity ( $\text{mA h g}^{-1}$ )                        | 3861   | 1165  | 685   | 2205  | 1337   | 820    |
| Theoretical volumetric capacity ( $\text{mAh cm}^{-3}$ ) | 2262   | 1128  | 610   | 3833  | 2073   | 5855   |
| Cost (US\$ ton $^{-1}$ )                                 | 165000 | 200   | 1000  | 4600  | 110000 | 2570   |

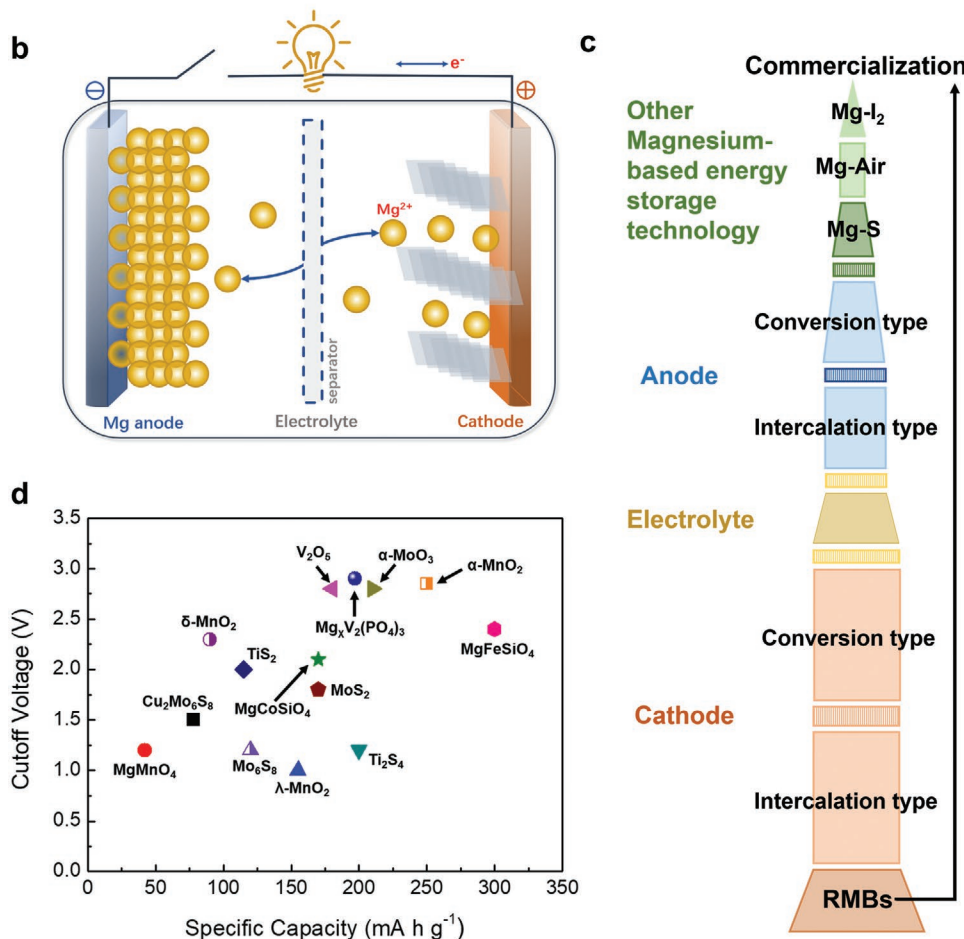


**Figure 1.** a) Comparison of various characteristics of magnesium metal with other metallic anodes.<sup>[29–32]</sup> b) The working principle and c) configuration of the rechargeable magnesium-ion battery. d) Capacities versus cut-off voltages of various cathode materials for rechargeable magnesium-ion batteries.

Mo sites, hindering further  $\text{Mg}^{2+}$  intercalation. The Mo sites reopen once the accumulated surface  $\text{Mg}_x\text{Cl}_y^+$  species transform into the neutral  $\text{MgCl}_2$  and release from surface adsorbates. This is impossible for other transitional metal oxides. This result verified the advantages of Chevrel phase as cathode materials for RMBs, compared with other materials.

Overall, the low working voltage and capacity of the Chevrel phase materials still hinder their further applications as cathode materials for RMBs. To solve these problems, it is essential to conduct an in-depth investigation on structure evolution, charge transfer mechanisms, reaction kinetics and irreversible  $\text{Mg}^{2+}$  trapping of  $\text{Mo}_6\text{S}_8$  CPs during Mg intercalation.

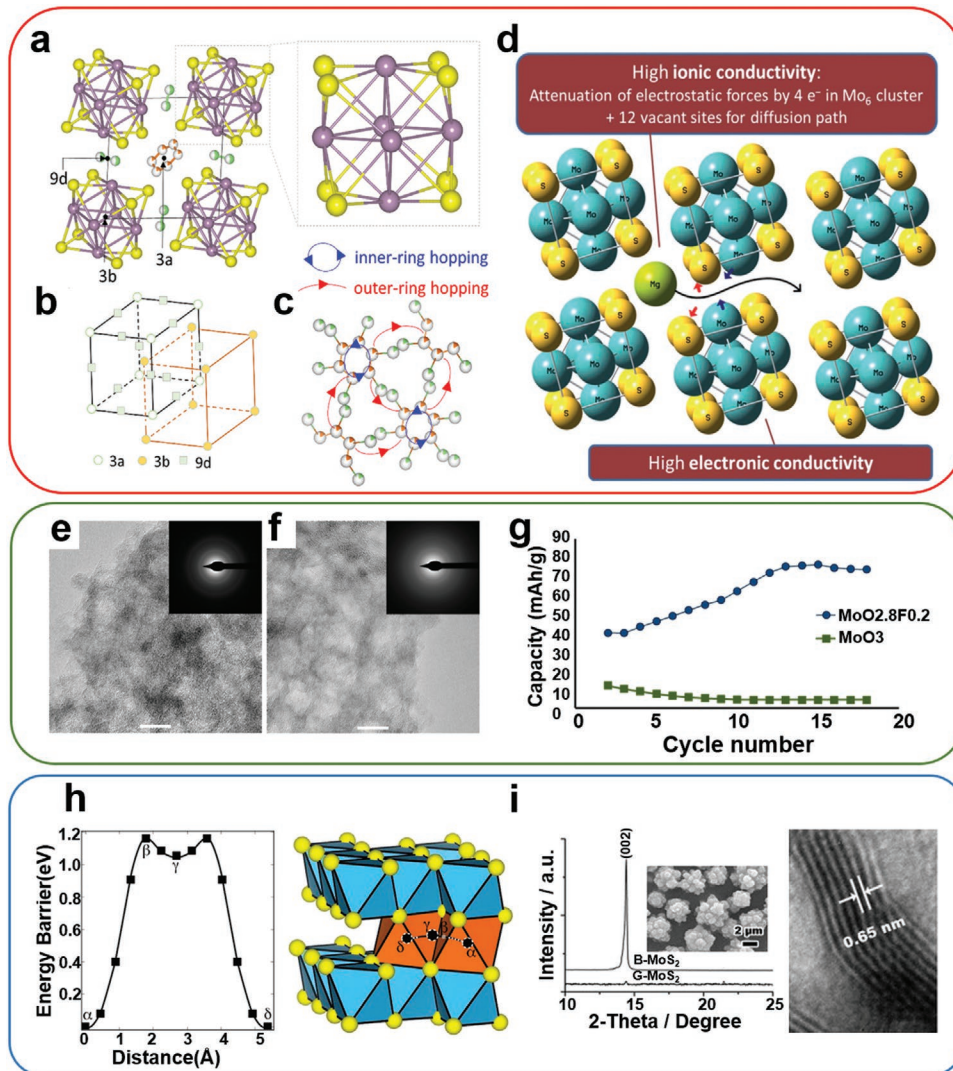


**Figure 2.** a) Crystal models of Chevrel phase (**CP**)  $\text{Mo}_6\text{S}_8$  with highly symmetric 3a, 3b, and 9d sites (viewed along the [211] direction). b) Sublattice of 3a and 3b sites. c) Inner-ring and outer-ring hopping between partially occupied outer and inner sites. Reproduced with permission.<sup>[49]</sup> Copyright 2017, American Chemical Society. d) Schematic illustration of solid-state diffusion of  $\text{Mg}^{2+}$  in the Chevrel phase (**CP**). Reproduced with permission.<sup>[19]</sup> Copyright 2012, The Royal Society of Chemistry. TEM images of e) magnesiated, and f) demagnesiated RBC/V<sub>2</sub>O<sub>5</sub> composites. Reproduced with permission.<sup>[59]</sup> Copyright 2016, Wiley-VCH Verlag GmbH & Co. KGaA. g) Capacity retention of  $\text{MoO}_2\text{F}_{0.2}$  and  $\text{MoO}_3$  electrodes versus the cycle number. Reproduced with permission.<sup>[63]</sup> Copyright 2015, American Chemical Society. h) Crystal structure and migration barrier of the layered  $\text{TiS}_2$ . Reproduced with permission.<sup>[67]</sup> Copyright 2015, American Chemical Society. i) XRD patterns and HRTEM images of G-MoS<sub>2</sub>. Reproduced with permission.<sup>[72]</sup> Copyright 2010, Wiley-VCH Verlag GmbH & Co. KGaA.

Additionally, other intercalation materials with higher voltage and charge storage capacity are encouraged to be discovered and developed. Meanwhile, the compatibility between cathodes and electrolytes should also be considered.

#### 2.1.2. Layered Structure Cathode Materials

Layered structure materials with unique 2D channels have huge potential in energy storage applications. Their special 2D characters provide abundant accessible chemical activity sites and endow them with fast insertion/extraction of ions, which contributes to rapid reaction kinetics and long-term

cycling.<sup>[53,54]</sup> Layered structure materials are of significant importance as electrode materials for alkaline rechargeable batteries such as LIBs and SIBs. Because of their weak van der Waals force, layered materials hold promise for  $\text{Mg}^{2+}$  intercalation as well.<sup>[16]</sup> Therefore, layered transitional metal oxides have been considered as one of the most promising cathode candidates for RMBs owing to their high working voltage, low cost, and structural flexibility (**Table 1**). For example, V<sub>2</sub>O<sub>5</sub>, which consists of layered edge and corner-sharing VO<sub>5</sub> pyramids, was confirmed to effectively accommodate large  $\text{Mg}^{2+}$ .<sup>[55,56]</sup> The reversible intercalation of  $\text{Mg}^{2+}$  into V<sub>2</sub>O<sub>5</sub>/carbon composites was reported by Imamura et al.<sup>[57]</sup> These composite materials showed a large interlayer spacing, which could shorten  $\text{Mg}^{2+}$

**Table 1.** Summary of layered structure cathode materials for RMBs.

| Cathode materials   | Discharge capacity                                      | Operating voltage | Capacity retention        | Electrolyte  | Refs. |
|---|---|-------------------|---------------------------|--|-------|
| $V_2O_5$ film   | 427 mAh g <sup>-1</sup> at 5.9 A g <sup>-1</sup>        | -1.5 V→1 V        | 82% after 2000 cycles     | 0.075 M MgCl <sub>2</sub>  | [58]  |
| $V_2O_5$ /RFC   | 350 mAh g <sup>-1</sup> at 40 mA g <sup>-1</sup>        | +0.5 V→2.8 V      | 65% after 100 cycles      | 0.2 M [Mg <sub>2</sub> (μ-Cl) <sub>2</sub> (DME) <sub>4</sub> ][AlCl <sub>4</sub> ] <sub>2</sub> in DME          | [59]  |
| $\zeta$ - $V_2O_5$  | 96.55 mAh g <sup>-1</sup> at 0.02 C                     | +0.2 V→3.4 V      | ≈64.3% after 100 cycles   | 0.2 M Mg(TFSI) <sub>2</sub>  | [60]  |
| $\alpha$ -MoO <sub>3</sub>                                      | 210 mAh g <sup>-1</sup> at 0.3 $\mu$ A cm <sup>-2</sup> | +2.2 V→2.8 V      | ≈83.3% after 30 cycles    | 0.5 M Mg(ClO <sub>4</sub> ) <sub>2</sub>   | [62]  |
| $Mo_{2.5+\delta}VO_{9+\delta}$                                  | 397 mAh g <sup>-1</sup> at C/70                         | +1.7 V→3.2 V      | 59.2% after 15 cycles     | 0.5 M Mg[N(SO <sub>2</sub> CF <sub>3</sub> ) <sub>2</sub> ] <sub>2</sub> , Mg(TFSI) <sub>2</sub> in acetonitrile | [64]  |
| Birnessite-MnO <sub>2</sub>                                     | 231.1 mAh g <sup>-1</sup> at 100 mA g <sup>-1</sup>     | -0.6 V→0.8 V      | 62.5% after 10 000 cycles | 0.5 M Mg(ClO <sub>4</sub> ) <sub>2</sub>   | [65]  |
| TiS <sub>2</sub>  | 115 mAh g <sup>-1</sup> at 0.1 C                        | +0.2 V→1.8 V      | 46% after 40 cycles       | APC/THF electrolyte and APC/tetraglyme   | [67]  |
| Expanded TiS <sub>2</sub>                                       | 400 mAh g <sup>-1</sup> at 48 mA g <sup>-1</sup>        | 0 V→2 V           | 80% after 400 cycles      | 0.25 M [Mg <sub>2</sub> Cl <sub>3</sub> ] <sup>+</sup> [AlPh <sub>2</sub> Cl <sub>2</sub> ] <sup>-</sup> in THF  | [34]  |
| Graphene-like MoS <sub>2</sub>                                  | 170 mAh g <sup>-1</sup> at 20 mA g <sup>-1</sup>        | +0.5 V→3 V        | 95% after 50 cycles       | Mg(AlCl <sub>3</sub> Bu) <sub>2</sub>  | [72]  |
| MoS <sub>2</sub> /Carbon  | 213 mAh g <sup>-1</sup> at 50 mA g <sup>-1</sup>        | 0 V→2.4 V         | 39.6% after 50 cycles     | 0.4 M [Mg <sub>2</sub> Cl <sub>3</sub> ] <sup>+</sup> [AlPh <sub>2</sub> Cl <sub>2</sub> ] <sup>-</sup> in THF   | [73]  |
| MoS <sub>2</sub> /C-PNR   | 120 mAh g <sup>-1</sup> at 10 mA g <sup>-1</sup>        | 0 V→2.5 V         | 71% after 200 cycles      | 0.4 M Mg[B(OCH(CF <sub>3</sub> ) <sub>2</sub> ) <sub>4</sub> ] <sub>2</sub> in DME                               | [35]  |
| TiSe <sub>2</sub>   | 110 mAh g <sup>-1</sup> at 5 mA g <sup>-1</sup>         | +0.2 V→1.8 V      | 87% after 50 cycles       | 0.25 M Mg(AlCl <sub>2</sub> EtBu) <sub>2</sub> /THF  | [74]  |
| WSe <sub>2</sub>  | 203 mAh g <sup>-1</sup> at 50 mA g <sup>-1</sup>        | +0.3 V→3 V        | 83.5% after 50 cycles     | 0.25 M Mg(AlCl <sub>2</sub> EtBu) <sub>2</sub> /THF  | [75]  |
| Ti <sub>3</sub> C <sub>2</sub> T <sub>x</sub> /CTAB             | 300 mAh g <sup>-1</sup> at 50 mA g <sup>-1</sup>        | 0 V→2 V           | 66.8% after 250 cycles    | 0.4 M (PhMgCl) <sub>2</sub> -AlCl <sub>3</sub> /THF  | [76]  |
| 3D-Ti <sub>3</sub> C <sub>2</sub> T <sub>x</sub>                | 210 mAh g <sup>-1</sup> at 5 C                          | +0.3 V→2.85 V     | 29.3% after 60 cycles     | 0.4 M (PhMgCl) <sub>2</sub> -AlCl <sub>3</sub> /THF  | [77]  |
| Ti <sub>3</sub> C <sub>2</sub> T <sub>x</sub> /Carbon           | 198.7 mAh g <sup>-1</sup> at 10 mA g <sup>-1</sup>      | 0 V→2 V           | ≈85% after 400 cycles     | 0.4 M [Mg <sub>2</sub> Cl <sub>3</sub> ] <sup>+</sup> [AlPh <sub>2</sub> Cl <sub>2</sub> ] <sup>-</sup> in THF   | [78]  |
| Ti <sub>3</sub> C <sub>2</sub> T <sub>x</sub> /MoS <sub>2</sub> | 165 mAh g <sup>-1</sup> at 50 mA g <sup>-1</sup>        | 0 V→2 V           | 65.4% after 50 cycles     | 0.4 M (PhMgCl) <sub>2</sub> -AlCl <sub>3</sub> /THF  | [79]  |
| MXene-Ti <sub>3</sub> C <sub>2</sub> /MnO <sub>2</sub>          | 105 mAh g <sup>-1</sup> at 50 mA g <sup>-1</sup>        | 0 V→2 V           | 55.2% after 100 cycles    | -  | [80]  |

diffusion paths and thereby improve the electrochemical performance of  $V_2O_5$ /carbon cathode materials. In addition, the growth of layered  $V_2O_5$  thin films RMBs cathode materials via aerosol-assisted chemical vapor deposition (AACVD) has also been studied.<sup>[58]</sup> These materials demonstrated a high specific capacity of 427 mAh g<sup>-1</sup> with a capacity loss of 18% after 2000 cycles, suggesting excellent structural stability and good reversibility. The advantages of layered  $V_2O_5$  nanoclusters supported on the resorcinol and formaldehyde (RFC) framework as cathode materials for RMBs were investigated by Cheng et al. (Figure 2e,f).<sup>[59]</sup> They exhibited a high first discharge capacity of 180 mAh g<sup>-1</sup> at 40 mA g<sup>-1</sup> within the voltage range from 0.5 to 2.8 V. Furthermore, the authors proposed a surface-dominated pseudocapacitive storage of Mg<sup>2+</sup> as a molecular storage mechanism, which provides a new perspective for high energy-density RMBs. The metastable  $\zeta$ - $V_2O_5$  polymorph was also described for RMBs.<sup>[60]</sup> A capacity of 0.33 Mg<sup>2+</sup> per formula unit (96.55 mAh g<sup>-1</sup>) was achieved with an average working potential of 1.65 V (vs Mg/Mg<sup>2+</sup>). The enhanced electrochemical performance is originated from the metastable local coordination environments and smaller bandgap to mitigate the Mg<sup>2+</sup> diffusion barrier. However, the reaction kinetics are still unsatisfactory and can be further enhanced by reducing the particle sizes.

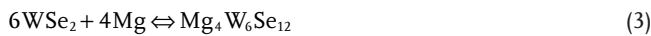
$MoO_3$  has also been recognized as a promising layered cathode material for RMBs and first reported by Spahr et al.<sup>[61]</sup> They identified that the fading mechanism was mainly ascribed to the structure evolution of the host material upon cycling. In addition, the abnormal cyclic voltammetry (CV) peaks implied unwanted side reactions caused by the interaction between electrode and electrolyte. In addition, the  $\alpha$ - $MoO_3$  film, which showed a high capacity of 210 mAh g<sup>-1</sup> between 2.2 and 2.8 V, was also reported as the cathode material for RMBs.<sup>[62]</sup> However, the overpotential was much higher than that for  $V_2O_5$  film,

suggesting obvious kinetic limitations. In order to enhance the electrochemical behavior of  $MoO_3$ , the incorporation of fluoride into the  $\alpha$ - $MoO_3$  structure via mild fluorination was done by Incorvati et al.<sup>[63]</sup> Figure 2g shows that  $MoO_{2.8}F_{0.2}$  delivered significantly higher specific capacity and better retention rate compared with the pristine  $\alpha$ - $MoO_3$  compound. Unlike the poor electrochemical performances of  $MoO_3$  observed in Figure 2g, the fluorinated  $\alpha$ - $MoO_{2.8}F_{0.2}$  increased the reaction kinetics over layered  $MoO_3$  and lowered the diffusion barrier for Mg<sup>2+</sup> migration. Orthorhombic molybdenum–vanadium oxides ( $Mo_{2.5+\delta}VO_{9+\delta}$ ) with the open and complex layer structure could also contribute to the improved Mg<sup>2+</sup> diffusion kinetics and cycling stability.<sup>[64]</sup> A high discharge capacity of 397 mAh g<sup>-1</sup> was obtained at C/70 at room temperature. Moreover, their microporous framework with unique ring tunnels ensures the rapid Mg<sup>2+</sup> diffusion and alleviates the volume expansion. Other layered transitional metal oxides have also been reported as intercalation hosts for RMBs. The incorporation of crystal water in layered Birnessite MnO<sub>2</sub> has been proven to be effective as an intercalation cathode material.<sup>[65]</sup> Crystal water can effectively shield the electrostatic interaction between Mg<sup>2+</sup> cations and host anions and minimize the impact of desolvation energy at the cathode–electrolyte interface in the nonaqueous electrolyte, thereby enhancing the structural stability. Moreover, in the aqueous electrolyte, the charge shielding effect decreases the interfacial energy and contributes to a high specific capacity of 231.1 mAh g<sup>-1</sup> and capacity retention up to 62.5% after 10 000 cycles.

Apart from the layered transitional metal oxides, layered transitional metal sulfides/selenides are also attractive as cathode materials for RMBs. As shown in Figure 2h, the typical layered TiS<sub>2</sub> composed of stacking sequences of TiS<sub>2</sub> slabs, where Ti atoms occupy octahedral sites and coordinate with close-packed

sulfur planes, and  $Mg^{2+}$  migrates between the stable octahedral and tetrahedral sites, which shows the unique structure for  $Mg^{2+}$  intercalation.<sup>[56,66,67]</sup> Sun et al.<sup>[68]</sup> reported layered  $TiS_2$  for nonaqueous Mg full cells, exhibiting a specific capacity of 115 mAh g<sup>-1</sup> at 0.1 C at 60 °C. Furthermore, XRD characterization revealed that the multistep  $Mg^{2+}$  insertion process is responsible for changes of  $Mg^{2+}$  siting, producing the inhomogeneous  $Mg^{2+}$  distribution in the particles. Moreover,  $TiS_2$  nanotubes could deliver a maximum discharge capacity of 115 mAh g<sup>-1</sup> with much better cyclability (a capacity loss of 0.65 mAh g<sup>-1</sup> per cycle), which is higher than polycrystalline  $TiS_2$ .<sup>[69]</sup> The  $MgCl^+$  intercalation mechanism in the expanded  $TiS_2$  cathode material has been proposed by Yoo and co-workers.<sup>[34]</sup> Owing to the expanded interlayer distance of  $TiS_2$  as well as the rapid diffusion kinetics of  $MgCl^+$ , the expanded  $TiS_2$  can deliver a specific capacity up to 400 mAh g<sup>-1</sup> at 60 °C outstanding rate capability and cycling stability. Another typical transition metal sulfide, layered  $MoS_2$  has also been reported as a cathode material for RMBs. Similar to  $TiS_2$ ,  $MoS_2$  2D structure contains Mo atom layers sandwiched by S atom layers. Single monolayer  $MoS_2$  stacks upon each other to form the bulk material.<sup>[70,71]</sup> Liang and co-workers<sup>[72]</sup> prepared graphene-like  $MoS_2$  (G- $MoS_2$ ) and their very weak (002) XRD peak and HRTEM image of G- $MoS_2$  (as shown in Figure 2i) indicated the highly exfoliated nature of the as-prepared material. When applied as cathode materials in RMB, it yielded a reversible specific capacity of 170 mAh g<sup>-1</sup> and an average operating voltage of 1.8 V. Such a monolayer structure shortens the  $Mg^{2+}$  ion diffusion path and benefits the improved electrochemical performances. Liu et al.<sup>[73]</sup> synthesized sandwich-structured  $MoS_2/C$  microspheres for RMBs through a hydrothermal method. The  $MoS_2/C$  cathode exhibited a higher discharge capacity of 118.8 mAh g<sup>-1</sup> after 20 cycles and better cycling stability than bare  $MoS_2$ . Furthermore, the rapid intercalation kinetics achieved by the solvated magnesium-ions bonded with dimethoxyethane ( $[Mg(DME)x]^{2+}$ ) was examined in the layered  $MoS_2$ .<sup>[35]</sup> The shielding effect of DME molecules represses the sluggish desolvation process on the interface between the cathode and electrolyte, and results in high  $Mg^{2+}$  mobility. Meanwhile, the intercalation process induces the phase transformation from 2H- $MoS_2$  to 1T- $MoS_2$ , which contributes to fast electron transfer and lowers the diffusion energy barrier for  $Mg^{2+}$  as well. Consequently, the cathode shows a high reversible capacity of 120 mAh g<sup>-1</sup> and excellent cycling stability after 200 cycles.

$TiSe_2$  cathode material with the hybridized electronic structure for RMBs.<sup>[74]</sup> The average specific capacity of  $TiSe_2$  is 108 mAh g<sup>-1</sup>, nearly 83% of its theoretical capacity (130 mAh g<sup>-1</sup>). They claimed that the charge delocalization via d-p orbital hybridization is the possible reason for intercalation/deintercalation of  $Mg^{2+}$  in this material. Liu et al.<sup>[75]</sup> synthesized a binder-free  $WSe_2$  nanowire-assembled film freestanding electrode for RMBs, which delivered a high specific capacity of 203 mAh g<sup>-1</sup> and remarkable capacity retention of 83.5% after 50 cycles. The charge-discharge reaction can be explained as



They further elucidated the  $Mg^{2+}$  intercalation behavior of  $WSe_2$  films through first-principles calculations, indicating that

more electrons preferred to transfer in the low energy filed. Overall, layered structure materials have gained much interest as cathode materials for RMBs owing to their favorable structure to achieve high operating voltage, high specific capacity and accessible sites for  $Mg^{2+}$  intercalation. However, such a structure is suffering from serve structure degradation and collapse during cycling, which greatly limits its future development. Strategies such as expanding the layer spacing and optimizing the particle size have been proved effective for further enhancing the cycling stability of layered structure materials and providing guidelines for developing high-performance RMBs cathode materials.

MXenes, which show high surface area, excellent cation intercalation capacity, and low ion diffusion barriers, have also been studied as the cathode materials for RMBs. For instance, the typical MXene  $Ti_3C_2$  was studied as cathode material for RMBs.<sup>[76]</sup> By preintercalating a cationic surfactant cetyltrimethylammonium bromide (CTAB) into delaminated (d)- $Ti_3C_2T_x$ , the diffusion barrier for  $Mg^{2+}$  ions on the MXene surface was reduced, enabling the reversible insertion/deinsertion of  $Mg^{2+}$  between adjacent MXene layers. As a result, the  $Ti_3C_2T_x/CTAB$  cathode delivered a high volumetric specific capacity of 300 mAh cm<sup>-3</sup> at 50 mA g<sup>-1</sup> and good cycling stability. In addition, 3D macroporous MXene films synthesized via a sacrificial template method has also been studied as cathode materials for RMBs.<sup>[77]</sup> The fabricated 3D macroporous films showed a high specific capacity of 210 mAh g<sup>-1</sup> at 5 C and remarkable rate capability especially at the high current rate. In comparison to the single MXene component, sandwich structured MXene@C nanocomposites has also been employed as cathode materials for RMBs.<sup>[78]</sup> Such a configuration significantly enlarged the interlayer spacing and provided abundant electrochemical active sites, which delivered a high specific capacity of 198.7 mAh g<sup>-1</sup> at 10 mA g<sup>-1</sup>, high rate capability, and outstanding cycling stability. Apart from carbon,  $MoS_2$  and  $MnO_2$  were incorporated into the MXene matrix via an one-step hydrothermal method.<sup>[79,80]</sup> The optimized composite structures not only enlarged the interlayer but also prevented MXene nanosheets from restacking.

### 2.1.3. Spinel Structure Cathode Materials

As shown in Figure 3a, the spinel structure shows the general formula of  $MgT_2X_4$  with the space group  $Fd\bar{3}m$ , where the octahedral cation (T) is coordinated by the cubic anion (X) in the packed lattice. Such an edge-sharing configuration gives rise to 3D diffusion paths (Figure 3a).<sup>[16]</sup> In contrast to the classical Chevrel phase (CP), spinel compounds have advantages such as high capacity and working voltage, which are promising to increase the energy density of RMBs. However, the  $Mg^{2+}$  diffusion energy barrier is quite high and, therefore, is unfavorable for reversible  $Mg^{2+}$  intercalation. To tackle these issues, many researchers devoted their efforts to the development of spinel structure cathode materials for RMBs. Sinha and Munichandraiah<sup>[81]</sup> first reported a spinel-like  $MgMnO_4$  by substituting  $Li^+$  in  $LiMn_2O_4$  as a RMB cathode material. Their study showed that the as-prepared  $MgMnO_4$  cathode material delivered a specific capacity of 42 mAh g<sup>-1</sup> and stabilized at 35 mAh g<sup>-1</sup> after

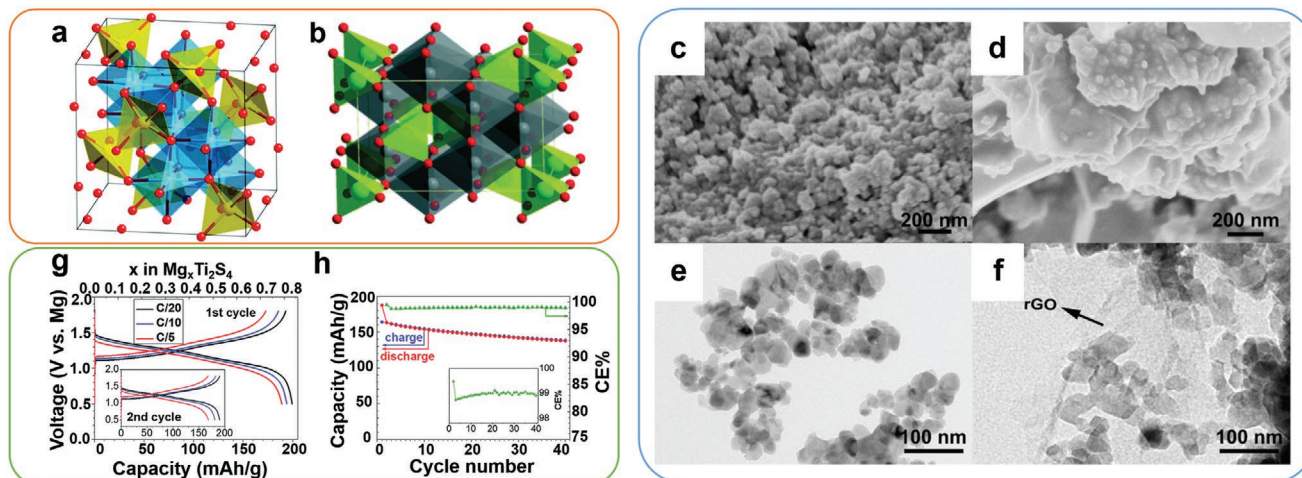


**Figure 3.** a) Crystal structure of spinel  $MgT_2X_4$ . Mg atoms are located at the yellow tetrahedral sites and the T atoms are located at the blue octahedral sites. Reproduced with permission.<sup>[16]</sup> Copyright 2018, The Royal Society of Chemistry. b) Crystal structure of spinel- $MnO_2$ . Reproduced with permission.<sup>[83]</sup> Copyright 2015, The Royal Society of Chemistry. SEM and TEM images of c,e) $MgMn_2O_4$  and d,f)  $MgMn_2O_4/rGO$ . Reproduced with permission.<sup>[84]</sup> Copyright 2018, The Royal Society of Chemistry. g,h) Galvanostatic discharge/charge voltage curves and cycling performance of  $C-Ti_2S_4$  cells with an APC electrolyte at 60 °C. Reproduced with permission.<sup>[86]</sup> Copyright 2016, The Royal Society of Chemistry.

20 cycles.  $\lambda$ - $MnO_2$  was also demonstrated as cathode materials for  $Mg^{2+}$  intercalation (Figure 3b).<sup>[82,83]</sup> It demonstrated an initial specific capacity of 545.6 mAh g<sup>-1</sup> and remained at 155.6 mAh g<sup>-1</sup> after 300 cycles. X-ray diffraction (XRD) and X-ray photoelectron spectroscopy (XPS) results also confirmed that  $\lambda$ - $MnO_2$  was transformed into spinel-like  $MgMn_2O_4$  after polarizing at -0.15 V. This phase transformation was likely to affect the mobility of  $Mg^{2+}$  in spinel-structured materials. Liu et al.<sup>[84]</sup> reported  $MgMn_2O_4/rGO$  nanocomposites for aqueous RMBs (Figure 3c-f). The as-prepared composite electrode showed a discharge capacity of 140.1 mAh g<sup>-1</sup> at a high current density of 1 A g<sup>-1</sup>, which is much higher than the bare  $MgMn_2O_4$  due to the enhancement of electronic conductivity through surface of the rGO film. Truong et al.<sup>[85]</sup> found that a thin rock-salt  $MgMn_2O_4$  layer was grown on the surface of cubic spinel  $MgMn_2O_4$  in non-aqueous electrolyte RMBs. The formation of the surface reconstruction layer was induced by Mg/Mn cation inter-exchange and Frenkel-defect-mediated relocation, enhancing the structural stability of the spinel phase for long-term cycling.

Several research groups also investigated spinel transition metal sulfides materials due to their higher  $Mg^{2+}$  mobility than its oxide counterparts and therefore facilitates outstanding electrochemical performance. For example, Nazar's group reported a thiospinel  $Ti_2S_4$  cathode material for RMBs.<sup>[86]</sup> Figure 3g,h shows that the resultant electrodes not only yielded a high specific capacity of 200 mAh g<sup>-1</sup> at a high operating voltage (1.2 V vs  $Mg^{2+}/Mg$ ) but also exhibited superior rate performance and cycling stability. Kolly and Van der Ven<sup>[87]</sup> predicted the crystal structure of spinel  $MgTi_2S_4$  using first-principle calculations and found the Mg-vacancy orderings could coordinate with Mg in both the octahedral sites and tetrahedral sites within spinel  $Mg_xTi_2S_4$ . Wustrow et al.<sup>[88]</sup> studied the electrochemical performance of thiospinel  $MgCr_2S_4$  and found although the  $Cr^{3+/4+}$  redox couple would contribute to a high working voltage, the oxidation of  $Cr^{3+}$  is quite difficult and, therefore, the removal of  $Mg^{2+}$  from the lattice is challenging. In summary, spinel compounds as cathodes for RMBs have an advantage in terms

of high capacity and working voltage. Furthermore, their unique structural stability during cycling can extend the cyclability. However, the sluggish  $Mg^{2+}$  diffusion kinetics and polarization effects still hamper their applications as cathode materials in RMBs. Optimizing nanostructures and tailoring intrinsic electronic structure are expected to alleviate these problems.

#### 2.1.4. Olivine Structure Cathode Materials

The polyanionic compounds with a 1D diffusion channel have achieved great success in energy storage devices.<sup>[89–91]</sup> For instance, the typical low-cost and environmentally-friendly olivine structured  $MgFeSiO_4$  consists of a hexagonal close-packed (hcp) oxygen configuration in which half of the octahedral sites are occupied by M (M = Fe, Mn, Co) or Mg ions, and one-eighth of the tetrahedral sites are occupied by Si ions.<sup>[16]</sup> Such a crystal structure effectively alleviates volume expansion and ensures structural stability during charge/discharge.<sup>[92,93]</sup> Therefore, a series of olivine structure cathode materials have been reported for RMBs. Oriksa et al.<sup>[94]</sup> presented ion-exchange synthesized  $MgFeSiO_4$  from  $Li_2FeSiO_4$  showed an attractive specific capacity over 300 mAh g<sup>-1</sup> at a potential of 2.4 V. Heath et al.<sup>[95]</sup> also used modeling techniques to systematically study the conduction of  $Mg^{2+}$ . As shown in Figure 4a, the  $Mg^{2+}$  migration energy and diffusion coefficient ( $D_{Mg}$ ) of  $MgFeSiO_4$  are 0.6 eV and  $10^{-9}$  cm<sup>2</sup> s<sup>-1</sup>, respectively, which are favorable for  $Mg^{2+}$  intercalation compared with other RMBs cathodes. DFT calculation predicts that the cell voltage for  $MgFeSiO_4$  is 2.35 V versus Mg/ $Mg^{2+}$ , which agrees well with current experimental results.

Mori and co-workers<sup>[96]</sup> prepared the olivine-type  $MgMnSiO_4$  via the flux method and calcinated at different temperatures. The low preparation temperature restricted the antisite mixing between Mn and Mg, which in turn endowed the electrochemical properties of this cathode material with a higher specific capacity. Characterized by the synchrotron XRD, the whole charge and discharge reaction underwent a single-phase

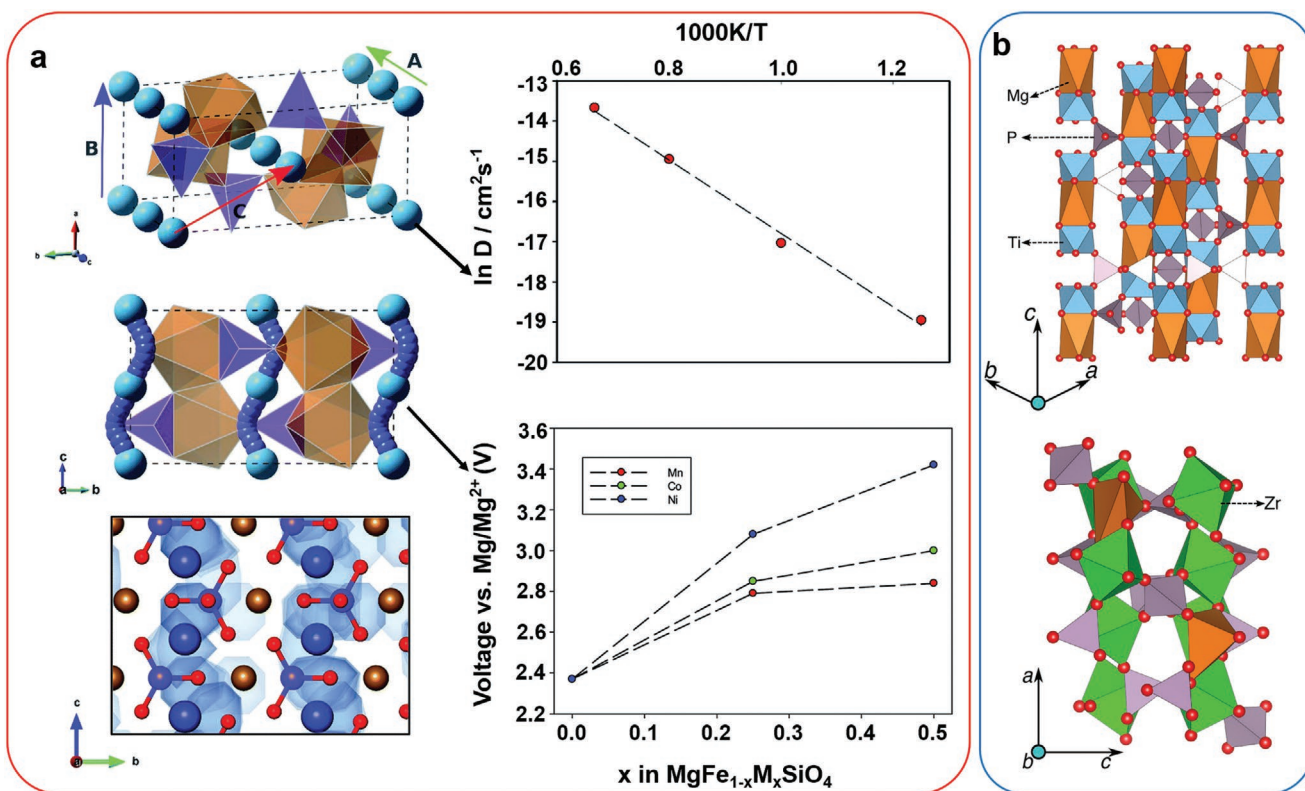


**Figure 4.** a) Crystal structure model, migration pathways, density plots and cell voltage from MD simulations of  $\text{MgFeSiO}_4$ . The results show the enhanced intercalation  $\text{Mg}^{2+}$  intercalation kinetics. Reproduced with permission.<sup>[95]</sup> Copyright 2017, The Royal Society of Chemistry. b) The hexagonal and monoclinic structure models of NASICON. Reproduced with permission.<sup>[11]</sup> Copyright 2017, American Chemical Society.

reaction and, consequently, charges were compensated by the change in the valence state of the olivine-type material. Truong et al.<sup>[97]</sup> synthesized nanocrystalline  $\text{MgMnSiO}_4$  through a rapid supercritical fluid method. The resultant small crystallite size demonstrated a shortened  $\text{Mg}^{2+}$  diffusion path and suppressed adverse antisite cation exchange. The control of grain sizes, as well as synthesis strategies for targeted particle morphologies of cathode materials, paved the way to boost the electrochemical performance of RMBs. In addition, mesoporous  $\text{MgCoSiO}_4$  cathode materials, prepared by the nonsurfactant mixed solvothermal method, showed a high initial discharge capacity of 170 mAh g<sup>-1</sup>, excellent rate capability and cyclability in the 0.25 mol L<sup>-1</sup>  $\text{Mg}(\text{AlCl}_2\text{EtBu})_2/\text{THF}$  electrolyte.<sup>[98]</sup> The improved electrochemical performances are ascribed to the large surface area, thin pore walls and abundant active sites for electrochemical reactions. Furthermore, the electrochemical properties are related to particle size and morphology of the cathode material. The formation of 3D hierarchical  $\text{MgCoSiO}_4$  was also reported for RMBs.<sup>[99]</sup> The unique 3D hierarchical open network contributed to reversible  $\text{Mg}^{2+}$  intercalation. Such an interconnected structure shortened the  $\text{Mg}^{2+}$  diffusion distance and facilitated electrolyte penetration.

#### 2.1.5. NASICON Structure Cathode Materials

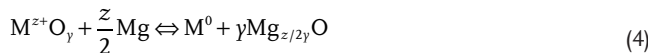
NASICON (natrium super ionic conductor) is a large family of materials with a similar structure to  $\text{Na}_{1+x}\text{Zr}_2\text{Si}_x\text{P}_{3-x}\text{O}_{12}$ . They usually have high ionic conductivities (on the order of  $10^{-3}$  S cm<sup>-1</sup>).<sup>[100]</sup>

Meanwhile, NASICON structured cathode materials provide enough space for  $\text{Mg}^{2+}$  intercalation and are good for structural stability (Figure 4b).<sup>[11,101–103]</sup> Makino et al.<sup>[104]</sup> illustrated NASICON-structured  $\text{Mg}_{0.5}\text{Ti}_2(\text{PO}_4)_3$  prepared by the sol-gel method and used it as a RMB cathode material in 1 M  $\text{Mg}(\text{ClO}_4)_2$  solution. Although  $\text{Mg}^{2+}$  could be reversibly intercalated and deintercalated in  $\text{Mg}_{0.5}\text{Ti}_2(\text{PO}_4)_3$ , its reversibility was still restricted by the diffusion and transport kinetics of  $\text{Mg}^{2+}$ . Therefore, they further studied the influence of  $\text{Fe}^{3+}$  and  $\text{Cr}^{3+}$  doping on the properties of  $\text{Mg}_{0.5}\text{Ti}_2(\text{PO}_4)_3$ .<sup>[105,106]</sup> It was found that doping elements could increase the  $\text{Mg}^{2+}$  conductivity without hindering its inherent advantages, thereby improving electrochemical performances. Another NASICON-type cathode material,  $\text{Mg}_x\text{V}_2(\text{PO}_4)_3$ , was synthesized through electrochemically delithiated from  $\text{Li}_3\text{V}_2(\text{PO}_4)_3$  by the use of a ball-milling-assisted solid-state carbothermal approach.<sup>[107]</sup> It exhibited a high specific capacity of 197 mAh g<sup>-1</sup> with an exceptional working potential (2.9 V) in 0.5 M  $\text{Mg}(\text{TFSI})_2$  acetonitrile solvent electrolyte. Such a high-voltage cathode material suggests that the electrochemical cation exchange method can be used for designing and synthesizing high performance cathode materials for RMBs.

#### 2.2. Conversion-Type Cathode Materials

Compared with intercalation compounds, the electrode based on the conversion reactions can achieve high theoretical capacity and energy density due to multielectrons contributions.

Conversion reactions normally occur in a situation when the cathode material does not have sufficient inserted sites or available diffusion channels.<sup>[16]</sup> In particular, the magnesiation and demagnesiation process involves the breaking of chemical bonds and formation of new phases as described below<sup>[108,109]</sup>



where M stands for the transitional metal. Hereinto, manganese oxide is one of the most representative conversion reaction-based electrode materials. In the structure, a  $MnO_6$  octahedron consisted with one Mn atom and six oxygen atoms, serves as the basic framework to construct different polymorphs of  $MnO_2$ .<sup>[110]</sup> Among them,  $\alpha$ - $MnO_2$  possesses the typical  $2 \times 2$  channel for ions transport and results in rapid kinetics. This feature makes  $\alpha$ - $MnO_2$  the promising candidate in LIBs,<sup>[111]</sup> SIBs,<sup>[112]</sup> and supercapacitors.<sup>[113]</sup> Considering its tunnel size ( $\approx 5 \text{ \AA}$ ) is much larger than that of  $Mg^{2+}$  (0.86  $\text{\AA}$ ), the transport and diffusion of  $Mg^{2+}$  in  $\alpha$ - $MnO_2$  is expected to be energetically favorable, and the reaction mechanisms behind  $\alpha$ - $MnO_2$  cathode materials are different from other type transitional metal oxides. Ling et al.<sup>[114]</sup> performed a comprehensive analysis with respect to the electrochemical behavior of  $\alpha$ - $MnO_2$ . They confirmed that the condition to generate amorphous  $Mg_xMnO_2$  is simpler than its intercalated product ( $\alpha$ - $Mg_xMnO_2$ ) through DFT calculation. Therefore, the conversion reaction was thermodynamically

preferable to the intercalation reaction. Although the conversion reaction played a dominant role during the magnesiation process, Mg is also intercalated below a concentration of  $\alpha$ - $Mg_{0.125}MnO_2$ . Another type  $\alpha$ - $MnO_2$  with a large surface area of  $70 \text{ m}^2 \text{ g}^{-1}$  was also prepared and discussed.<sup>[115]</sup> When tested on the Mg half-cell, it showed a first discharge capacity of  $250 \text{ mAh g}^{-1}$ . Their findings showed that the reaction process was dominated by the surface-controlled reaction. Zhang et al.<sup>[116]</sup> investigated the electrochemical performance of  $\alpha$ - $MnO_2$  as a cathode material for RMBs. Although it showed a high reversible initial discharge capacity of  $240 \text{ mAh g}^{-1}$ , the partial collapse of the original tunnel structure, caused by the breakage of the  $MnO_6$  octahedra, resulting into the irreversibility and structural instability with serious capacity decay in subsequent cycles. As characterized by a synchrotron-based X-ray absorption spectroscopy (XAS) in the transmission mode (Figure 5a), the K edge position of Mg did not fully recover to its original state after cycling, implying the partial irreversibility at the end of discharge, which leads to the irreversible capacity loss.

Apart from  $\alpha$ - $MnO_2$ , birnessite-type  $MnO_2$  composed of stacked  $MnO_6$  octahedron as well as structural water shows great potential for application in RMBs. Its large 2D diffusion path with an interlayer distance of  $7 \text{ \AA}$  facilitates the  $Mg^{2+}$  diffusion.<sup>[117,118]</sup> Sun et al.<sup>[117]</sup> synthesized the layered birnessite-phase  $MnO_2$  on the carbon cloth (Mg-bir/CC) and evaluated its electrochemical performance as the RMB cathode material. SEM and TEM images (Figure 5b,c) show the  $MnO_2$  sheets were

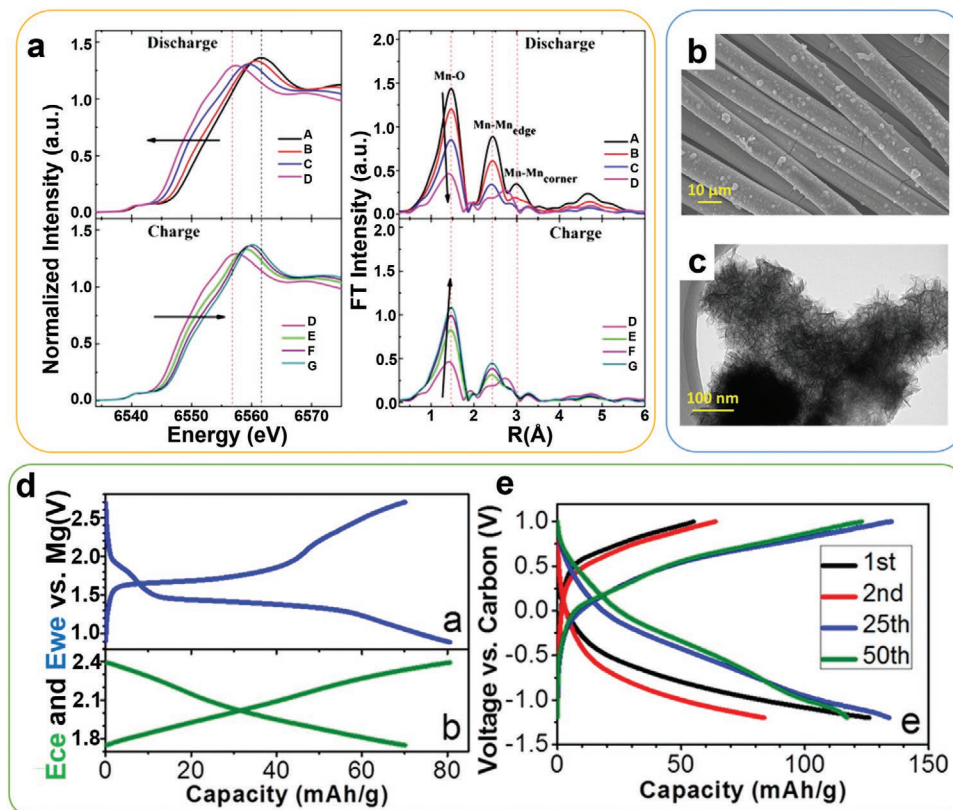


**Figure 5.** a) X-ray near edge absorption structure (XANES) and X-ray absorption fine structure (EXAFS) spectra for  $\alpha$ - $MnO_2$  in various discharge/recharge states. Reproduced with permission.<sup>[116]</sup> Copyright 2012, Elsevier. b,c) SEM and TEM images of Mg-bir/CC electrodes. Electrochemical performances of Mg-bir/CC electrodes: d) voltage profile and e) cycling performance at C/10 in 0.25 M  $Mg(TFSI)_2$ /diglyme electrolyte. Reproduced with permission.<sup>[117]</sup> Copyright 2016, American Chemical Society.

directly grown on the surface of the carbon cloth. Figure 5d exhibits voltage plateaus at around 1.4 and 1.7 V during charge and discharge in 0.25 M Mg(TFSI)<sub>2</sub>/diglyme, respectively. Such flat plateaus indicate a conversion reaction mechanism took place, with the formation of MnOOH, MnO, and Mn(OH)<sub>2</sub> after discharge. A discharge capacity of 90 mAh g<sup>-1</sup> was obtained after 50 cycles at C/10 (Figure 5e), indicating good stability.

Recently, CuS is emerging as a promising cathode material for RMBs. For example, CuS nanoparticles have been introduced as high-performance cathode materials for RMBs.<sup>[119]</sup> The cathode materials exhibit a reversible specific capacity of 175 mAh g<sup>-1</sup> at 50 mA g<sup>-1</sup> and excellent cycling stability over 350 cycles. The improvement of electrochemical performance is mainly ascribed to nanosized CuS particles, which not only facilitate the diffusion kinetics but also prevent the materials from aggregating upon cycling. 2D CuS hierarchical nanosheets have also been reported as cathode materials for RMBs via a one-step microwave-assisted method.<sup>[120]</sup> Such a unique hierarchical microstructure provides abundant electrochemical reaction sites and mitigates the volume expansion during charge and discharge processes, showing a high discharge capacity of 300 mAh g<sup>-1</sup> at 20 mA g<sup>-1</sup>, excellent rate capability and long cycle life. Moreover, the magnesium storage properties in 3D CuS nanospheres were investigated by Xiong et al.<sup>[121]</sup> They demonstrated that the cathode material could deliver a high specific capacity of 361 mAh g<sup>-1</sup> in Mg(ClO<sub>4</sub>)<sub>2</sub>/AN electrolyte at room temperature via three-electrode system. In the full cells, the CuS cathode showed the highest discharge capacity of 165 mAh g<sup>-1</sup> with a voltage plateau at elevated temperature in APC/THF electrolyte (55 °C). They employed ex situ technologies to further confirm the conventional magnesium storage mechanism of CuS nanospheres.

### 3. Anode Materials

Although one of the most attractive features for RMBs is the employment of low-cost, earth-abundant and dendrite-free metallic Mg as the anode, which results in a high Coulombic efficiency close to 100% under a suitable condition.<sup>[10,94,122]</sup> Early findings show that one of the most serious problems is the irreversible formation of a passivation layer on the surface of the Mg anode, which blocks the diffusion channel for Mg<sup>2+</sup> ions and therefore hinders reversible plating and stripping of Mg<sup>2+</sup>.<sup>[19,123,124]</sup>

Recently, replacing Mg metal with other anode materials has raised expectations for opportunities to develop high-performance RMBs. However, many anode materials cannot electrochemically react with metallic Mg due to the particular reaction mechanisms of the Mg<sup>2+</sup> cation. Wu et al.<sup>[125]</sup> introduced the spinel Li<sub>4</sub>Ti<sub>5</sub>O<sub>12</sub> (LTO) as an intercalation-based anode material for RMBs with a reversible specific capacity of 175 mAh g<sup>-1</sup>, corresponding to 1.5 Mg per formula unit. The low-strain characteristic of LTO results in remarkable cycling stability, as illustrated by the negligible capacity decay over 500 cycles. Additionally, the mesoporous Li<sub>3</sub>VO<sub>4</sub>/carbon (LVO/C) was also reported as the intercalation-type anode material for RMBs.<sup>[126]</sup> It showed an initial specific capacity of 318 mAh g<sup>-1</sup> and remarkable cycling stability as well. A unique hollow

structure with a large specific surface area effectively shortens the diffusion path for Mg<sup>2+</sup> and enhances the electrochemical performance. Meng and co-workers<sup>[127]</sup> prepared TiO<sub>2</sub>-B nanowires exposed with the (-110) facets, making Mg<sup>2+</sup> ions coordinated with unpaired surface oxygen atoms to achieve a high specific capacity of 110 mAh g<sup>-1</sup> at 0.1 C and a negligible capacity loss of 0.08% per cycle.

Alloying-based anode materials have been extensively studied owing to their high theoretical specific capacity. For example, a high-energy-density Sn anode for RMBs was based on the alloying mechanism.<sup>[128]</sup> The anode exhibited a very high specific capacity of 903 mAh g<sup>-1</sup>. Moreover, they also highlighted the compatibility of the Sn anode with Mo<sub>6</sub>S<sub>8</sub> cathode in the full cell, emphasizing the practical application of Sn anode material for RMBs. Parent et al.<sup>[129]</sup> investigated the Mg<sup>2+</sup> diffusion mechanism in nanostructured Sn via scanning transmission electron microscopy (STEM) and ab initio modeling (Figure 6a) and found that the electrochemical performance of Sn highly relies on the sizes and morphologies of Sn nanoparticles (<40 nm). Apart from Sn, Bi is also an important alloying-based anode for RMBs. Shao et al.<sup>[130]</sup> revealed the reversible conversion reaction of Mg<sup>2+</sup> in nanostructured Bi for RMBs. The nanostructured Bi could alleviate volume expansion and shorten the Mg<sup>2+</sup> diffusion distance, showing a high specific capacity of 350 mAh g<sup>-1</sup>, high initial Coulombic efficiency (~95%), and outstanding stability. Mg<sub>3</sub>Bi<sub>2</sub> alloy nanoclusters showed a discharge capacity of 360 mAh g<sup>-1</sup> associated with high Coulombic efficiency and long cycling life at the current rate of 0.1 A g<sup>-1</sup>.<sup>[123]</sup> Figure 6b demonstrates a two-phase conversion reaction of the Mg<sub>3</sub>Bi<sub>2</sub> alloy during charge and discharge. When the nanoclustered Mg<sub>3</sub>Bi<sub>2</sub> anode associated with Prussian Blue to assemble a full cell, it showed an initial discharge capacity of 101 mAh g<sup>-1</sup> with a capacity retention of 88% after 200 cycles (Figure 6c,d). Furthermore, a novel dual phase Bi-Sn alloy with exceptional magnesium storage behavior was proposed for RMBs.<sup>[131]</sup> The Bi<sub>6</sub>Sn<sub>4</sub> anode delivered reversible specific capacity (434 mAh g<sup>-1</sup> at 50 mA g<sup>-1</sup>), remarkable cycling stability (68% capacity retention) and improved rate capability (362 mAh g<sup>-1</sup> at 1 A g<sup>-1</sup>). Ex situ XRD and TEM confirmed the consistent structural evolution of Bi<sub>6</sub>Sn<sub>4</sub> anode during charge and discharge. The increased phase/grain boundaries are of great importance to accommodate large volume change and reduce the Mg<sup>2+</sup> diffusion length. Overall, although many achievements have been made in the development of anode materials for RMBs, their specific capacities are still lower than that of metallic Mg. Therefore, it is highly demanded to exploit anode materials with high discharge capacity and low intercalation potential for rechargeable magnesium-ion batteries.

### 4. Other Magnesium Energy Storage Technology

#### 4.1. Mg-Air Batteries

Metal-air batteries such as lithium-air<sup>[131,132]</sup> and zinc-air batteries<sup>[133]</sup> are attracting much attention as promising energy storage devices thanks to their low cost and high energy density. Furthermore, the utilization of oxygen from the air as the main reactant for metal-air batteries can significantly reduce the weight of the battery, as indicated in Figure 7a. Rechargeable

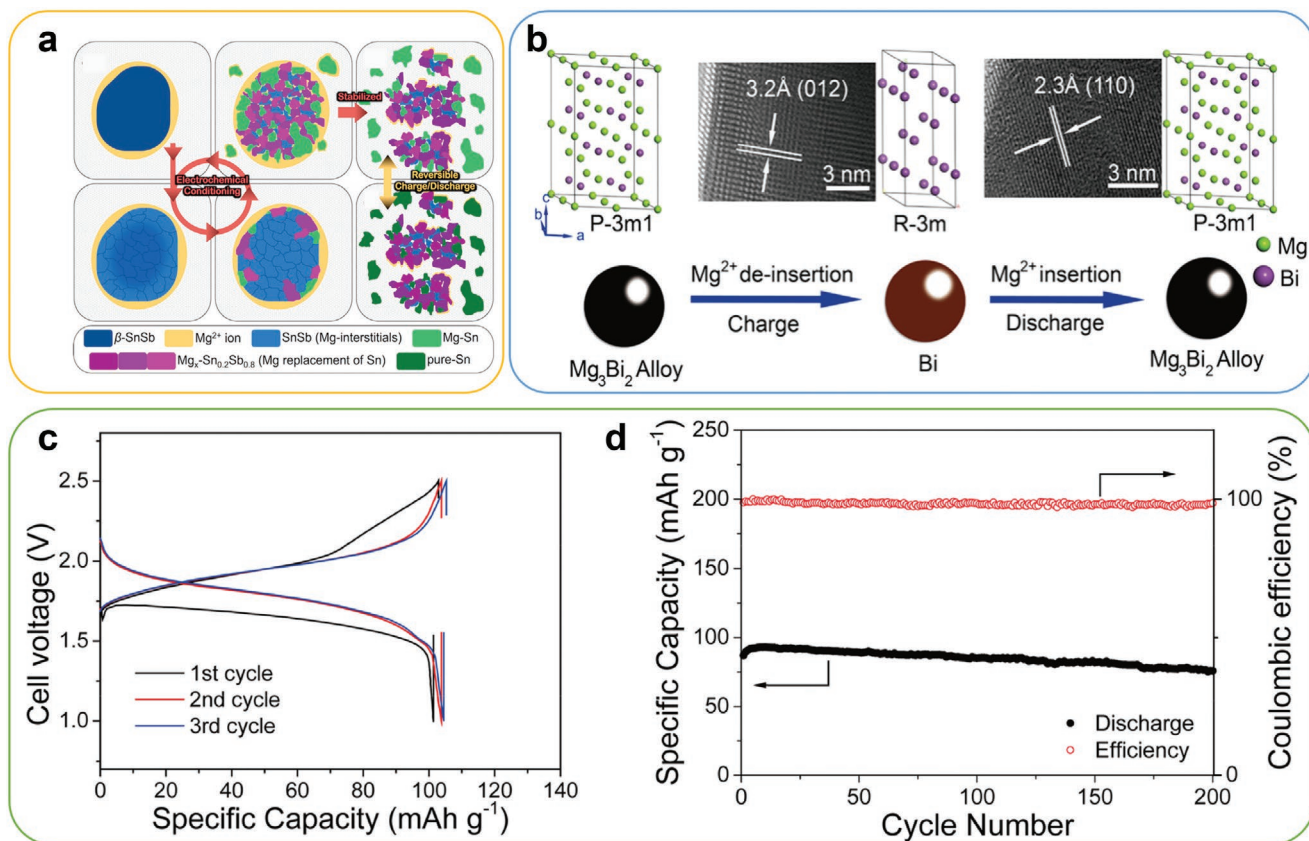


**Figure 6.** a) Diagram of the Mg<sup>2+</sup> intercalation and deintercalation processes of β-SnSb nanoparticles according to the TEM and DFT results. Reproduced with permission.<sup>[129]</sup> Copyright 2015, American Chemical Society. b) Schematic illustration of a two-phase conversion reaction of Mg<sup>2+</sup> ions in the Mg<sub>3</sub>Bi<sub>2</sub> alloy. c) Galvanostatic discharge/charge voltage curves and d) the cycling performance of full cells with 1 M LiTFSI–2 M Mg(TFSI)<sub>2</sub>/AN electrolyte. Reproduced with permission.<sup>[123]</sup> Copyright 2018, American Chemical Society.

Mg-air batteries show many advantages, such as a high working voltage (3.09 V) and high energy density (3910 Wh kg<sup>-1</sup>).<sup>[134,135]</sup> However, the corrosion of metallic Mg generates H<sub>2</sub> and therefore limits the faradaic efficiency, which is the main problem that hinders the further development of Mg-air batteries.<sup>[135]</sup>

There are four types of Mg-air batteries: primary Mg-air batteries,<sup>[136]</sup> Mg<sub>2</sub>Ni-air batteries,<sup>[137]</sup> Mg-air batteries with an organic electrolyte<sup>[138]</sup> and Mg-air batteries with a hybrid electrolyte. In the primary Mg-air battery with aqueous electrolyte, Mg anode is not compatible with aqueous electrolytes due to the self-corrosion of metallic Mg, leading to the generation of insulated Mg(OH)<sub>2</sub>. Richey et al.<sup>[139]</sup> reported Mg corrosion in different electrolytes and observed a higher H<sub>2</sub> evolution rate in NaCl than in NaNO<sub>3</sub>. Therefore, the problem of self-corrosion could be solved by using a new electrolyte. The metal hydride-air (MH-air) batteries have the merits of both Ni-MH batteries and metal-air batteries. The reactions of the charge and discharge processes in MH-air batteries are<sup>[140]</sup>



Although the MH-air battery shows better electrochemical performance and much safer than the primary Mg-air battery, the heavy mass of Ni(OH)<sub>2</sub> cathode would limit their further applications. Compared to the first two Mg-air battery systems, Mg-O<sub>2</sub> batteries have gradually drawn researchers' attention owing to their high theoretical volumetric energy density and theoretical capacity. In nonaqueous electrolytes, O<sub>2</sub> was first reduced to O<sup>2-</sup> and then generated solid MgO<sub>2</sub> and MgO. However, the precipitation of MgO was often uneven due to the high charging voltage. In order to achieve uniform MgO precipitation, Shiga et al.<sup>[141]</sup> utilized the iodine-dimethylsulfoxide and 2,2,6,6-tetramethylpiperidine-oxyl-anion complexes as electrocatalysts for air cathodes to facilitate the homogenous precipitation of MgO. Mn<sub>3</sub>O<sub>4</sub> nanowires/3D graphene/single-walled carbon nanotubes (Mn<sub>3</sub>O<sub>4</sub> nanowires/3D GN/SWCNT) were also introduced as catalysts for Mg-air batteries.<sup>[142]</sup> Figure 7b shows a typical XRD pattern of Mn<sub>3</sub>O<sub>4</sub> nanowires/3D GN/SWCNT. Compared with the bulk 3D GN/SWCNT microstructure, Mn<sub>3</sub>O<sub>4</sub> nanowires with diameters of 8–30 nm were grown on the graphene to form an open 3D nanonetwork architecture (Figure 7c–f). The Mn<sub>3</sub>O<sub>4</sub> nanowires/3D GN/SWCNT framework showed improved ionic conductivity and anode activity (Figure 7g).

The Mg-air battery with hybrid electrolyte is composed of the Mg anode, an air cathode and the saline electrolyte. The Mg anode can produce two electrons, thus being oxidized to Mg<sup>2+</sup>,

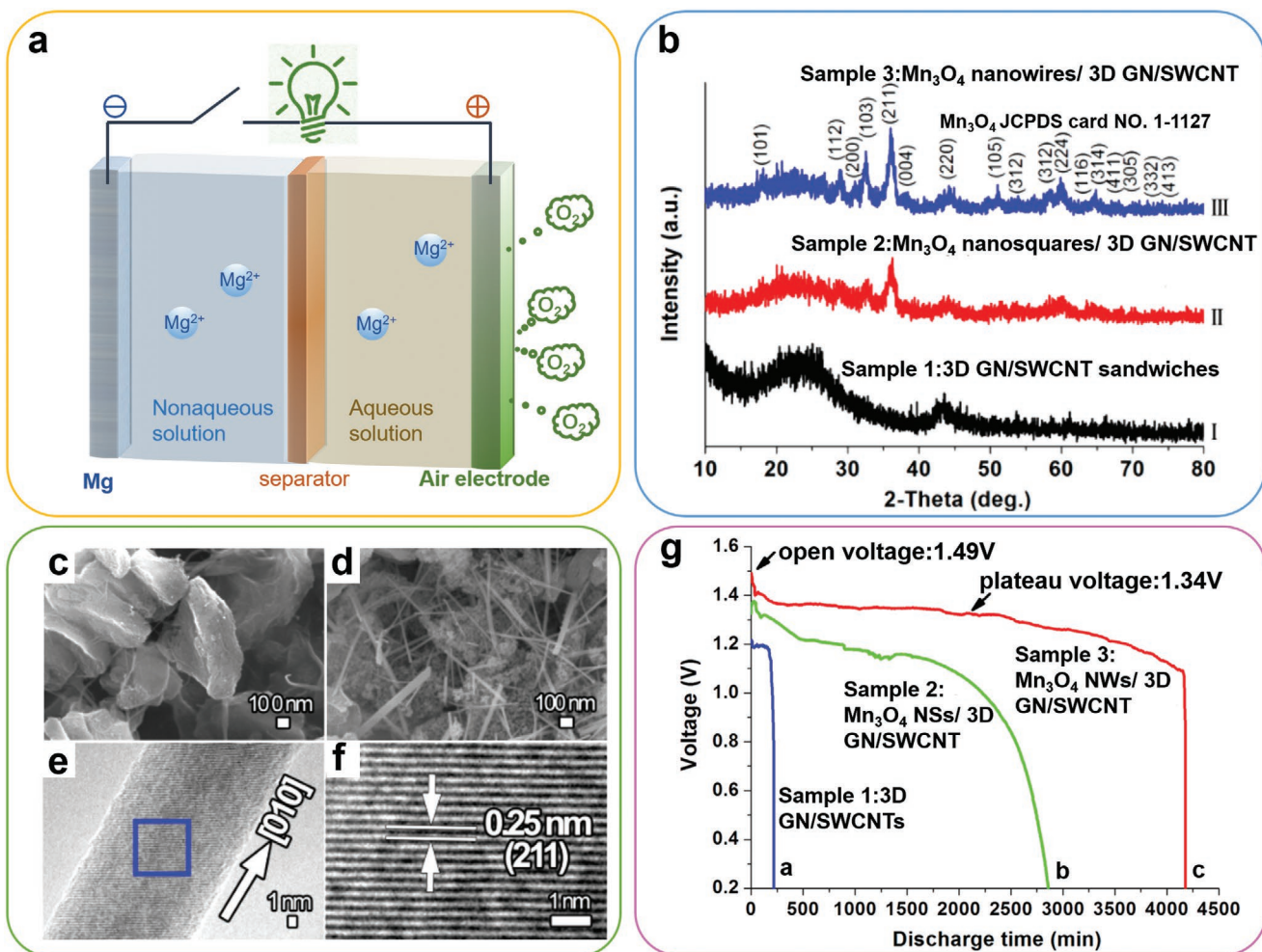
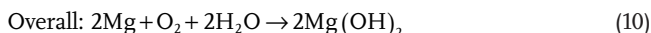


**Figure 7.** a) Typical structure and working principle of the Mg–air battery. b) XRD patterns of three different Mg anode samples. c–f) SEM and TEM images of the commercial 3D GN/SWCNT microstructure and the Mn<sub>3</sub>O<sub>4</sub> nanowires/3D GN/SWCNT composite. g) Galvanostatic discharge/charge profiles of different Mg-air batteries measured at a current density of 0.2 mA cm<sup>-2</sup> with a mixed electrolyte of Mg(NO<sub>3</sub>)<sub>2</sub> (2.6 M) and NaNO<sub>2</sub> (3.6 M) and different amounts of [P6,6,14][Cl] ionic liquid: a) 0.5, b) 1.0, and c) 2.0 wt%. Reproduced with permission.<sup>[142]</sup> Copyright 2016, American Chemical Society.

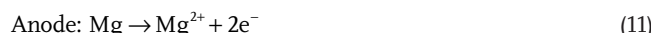
while O<sub>2</sub> reacts with H<sub>2</sub>O and electrons to generate OH<sup>−</sup>. The charge and discharge reactions in Mg-air batteries with hybrid electrolyte are<sup>[135]</sup>



It should be indicated that practical Mg-air batteries have so far been primary batteries. The large-scale application of rechargeable Mg-air batteries still requires further exploration. Given to the partial irreversibility of magnesium oxide, magnesium peroxide has been proposed to be a good choice owing to its higher activity. Searching for stable electrolyte is the key point for the cycling stability of Mg-air batteries. Finally, electrocatalysts should not only be chemically active for both the oxygen evolution and reduction reactions, but also reduce cell polarization and thus accelerate the decomposition of discharge products.

#### 4.2. Mg-Sulfur Batteries

Mg-sulfur batteries are starting to attract interests because of the abundant raw materials for both anode and cathode materials. Furthermore, Mg-sulfur batteries theoretically show better electrochemical performance than their lithium-sulfur counterparts because metallic magnesium does not form dendrites during the charge and discharge processes. As shown in Figure 8a, the typical Mg-sulfur battery consists of the Mg anode, the organic electrolyte and a sulfur cathode. The reactions of the charge and discharge in Mg-sulfur batteries are



Unlike the direct use of metallic Mg anode in Mg-sulfur batteries, the development of cathode materials for Mg-sulfur batteries is still in infancy.<sup>[143]</sup> The most commonly used cathode

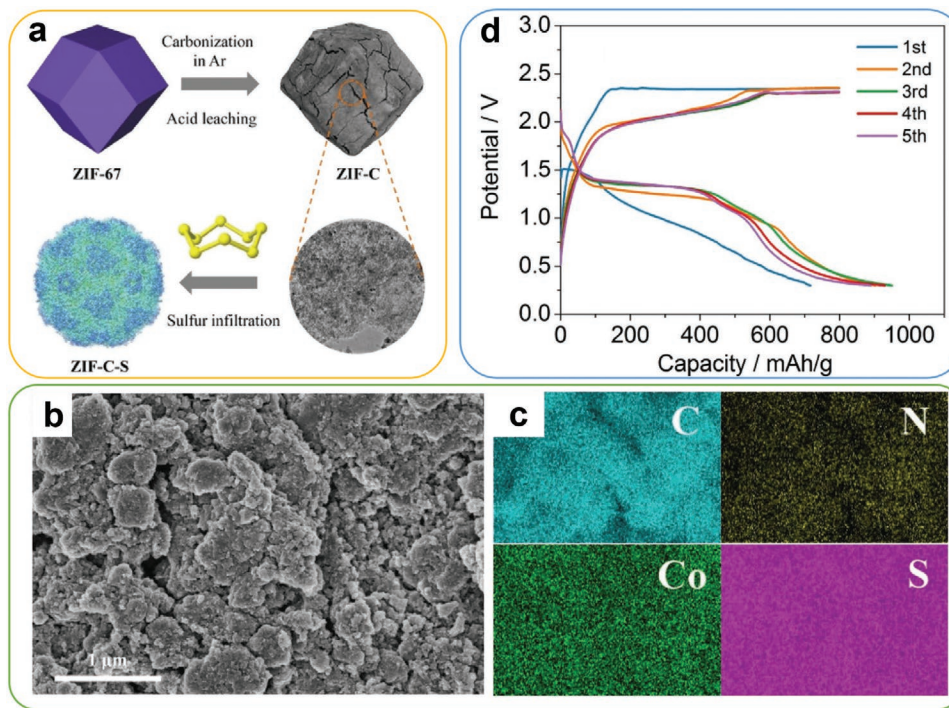


**Figure 8.** a) Schematic illustration of the preparation of ZIF-C and ZIF-C-S. b) SEM image and c) corresponding EDX mapping images of ZIF-C-S. d) Galvanostatic discharge/charge profiles of ZIF-C-S at 0.1 C in  $(\text{HMDS})_2\text{Mg}-\text{AlCl}_3-\text{LiTFSI}$  electrolyte. Reproduced with permission.<sup>[149]</sup> Copyright 2018, Wiley-VCH Verlag GmbH & Co. KGaA.

materials were a mixture of sulfur powder and carbon black or acetylene black. Recently, 2D materials with appropriate sulfur-loading were trialed as cathode materials to improve the electrochemical performance of Mg-sulfur batteries. However, the major issue for developing Mg-sulfur batteries is related to the notorious shuttle effects. This phenomenon caused by the dissolution and migration of polysulfide species during cycling can accelerate the capacity fading of the batteries.<sup>[144–146]</sup> Meanwhile, the generation of discharge products such as  $\text{MgS}$  and  $\text{Mg}_2\text{S}_8$  through intermediate polysulfide leads to capacity degradation.<sup>[147]</sup> As a consequence, many pioneering works have been devoted to tackling the dissolution and migration of polysulfide species for Mg-sulfur batteries. Vinayan et al.<sup>[148]</sup> reported a mixture of graphene and sulfur as the cathode material for Mg-sulfur batteries. The initial discharge capacity was 1024 mAh g<sup>-1</sup> but decreased to 236 mAh g<sup>-1</sup> after 50 cycles. Meanwhile, the metal-organic framework with ultrahigh surface area and tunable structural topology were also employed as cathode materials to improve the electrochemical performance of Mg-sulfur batteries. Zhou et al.<sup>[149]</sup> took advantage of ZIF-67 as a precursor to produce nitrogen and cobalt codoped functional carbon scaffolds as cathode materials (Figure 8a). SEM and corresponding energy-dispersive X-ray (EDX) mapping images of ZIF-C-S in Figure 8b,c confirm the homogenous distribution of C, N, Co, and S elements. The ZIF-C-S electrode delivered a high discharge capacity of 800–900 mAh g<sup>-1</sup> during the first five cycles. Replacing metallic Mg with alloy-type  $\text{Mg}_3\text{Bi}_2$  in  $\text{Mg}(\text{TFSI})_2$ -based electrolyte is expected to be an alternative approach.<sup>[150]</sup> The  $\text{Mg}_3\text{Bi}_2/\text{S}$  cell delivers a high discharge capacity more than 700 mAh g<sup>-1</sup> and low overpotential compared with metallic Mg

anode. Apart from cathode materials, the electrolyte is also an important component for achieving high-performance Mg-sulfur batteries. The first nucleophilic electrolyte was reported by Kim et al.<sup>[151]</sup> They found that the electrolyte containing a non-nucleophilic Mg-based complex in tetraglyme solvent such as Mg-bis(hexamethyldisilazide)[ $(\text{HMDS})_2\text{Mg}$ ] mixing with the Lewis acid,  $\text{AlCl}_3$  and tetraglyme ether-based solvent can achieve a significant improvement in Coulombic efficiency and stability of Mg-sulfur batteries. The electrochemical performances can be effectively improved by adding  $(\text{HMDS})_2\text{Mg}$  based diglyme and tetraglyme electrolyte with N-methyl-N-butylpiperidinium bis(trifluoromethanesulfonyl)imide (PP14TFSI) as an additive.<sup>[152]</sup> The employment of ionic liquid and glymes as solvents significantly boosts the electrochemical performance of the Mg/CMK/S cell. Such a non-nucleophilic based Mg-sulfur battery showed a large upper voltage plateau and higher capacity. However, the serious capacity loss due to large voltage hysteresis during cycling should be overcome. Considering this point, the effectiveness of non-nucleophilic borate-based electrolytes such as  $\text{Mg}[\text{B}(\text{OCH}(\text{CF}_3)_2)_4]_2$  and  $[\text{Mg}_4\text{Cl}_6(\text{DME})_6][\text{B}(\text{HFP})_4]_2$  for Mg-sulfur batteries was also studied.<sup>[153,154]</sup> The results showed that both  $\text{Mg}[\text{B}(\text{OCH}(\text{CF}_3)_2)_4]_2$  and  $[\text{Mg}_4\text{Cl}_6(\text{DME})_6][\text{B}(\text{HFP})_4]_2$  exhibited high conductivity, high oxidative stability, good chemical compatibility and excellent long-term durability, ensuring the reversibility and stability of sulfur cathode with high energy density. Gao et al.<sup>[155]</sup> revealed the reversible  $\text{S}^0/\text{MgS}_x$  redox chemistry in the  $\text{MgTFSI}_2/\text{MgCl}_2/\text{DME}$  electrolyte for Mg-sulfur batteries. They confirmed that serious voltage hysteresis is caused by the large Mg anode overpotential. In addition, the dissolution of polysulfide is effectively restricted through the

concentrated electrolyte solution and the chemical stability of the  $S^0/MgS_x$  process, which enables the long-term operation and safety of Mg-sulfur batteries.

#### 4.3. Mg-Iodine Batteries

For Mg-based batteries, iodine ( $I_2$ ) can serve as a suitable cathode material to kinematically enhance the  $Mg^{2+}$  diffusion and migration. This is because the intermediate product ( $Mg(I_3)_2$ ) is highly soluble, while the final product ( $MgI_2$ ) is insoluble.<sup>[156]</sup> Therefore, the shuttle effect and the presence of polyiodide can be mitigated in Mg-iodine batteries. Figure 9a shows a schematic illustration of rechargeable Mg-iodine batteries. In this system,  $I_2$  cathode is expected to exhibit rapid redox reaction kinetics than common intercalation cathodes and, therefore, provides high working voltage as well as specific capacity. Tian et al.<sup>[156]</sup> reported a new type of Mg-iodine battery using activated carbon cloth and aluminum chloride (ACC/ $I_2$ ) as the cathode and magnesium bis(trimethylsilyl)amide ((HMDS)<sub>2</sub>Mg) with magnesium chloride in tetraglyme as the electrolyte. As shown in Figure 9b, the SEM image

shows that there was no residual  $I_2$  on the surface of ACC/ $I_2$ . The as-prepared Mg-iodine battery showed an initial capacity of 200 mAh g<sup>-1</sup> at C/4 and a high energy density of 400 Wh kg<sup>-1</sup>. Furthermore, when the cell was cycled at C/2, the capacity retention was 94.6% after 120 cycles (Figure 9c). The rate capability of the as-prepared ACC/ $I_2$  cathode is much better than the previously reported RMB cathode materials (Figure 9d).

#### 5. Conclusion

The burgeoning demand for renewable energy storage inspires researchers to explore low-cost cutting-edge battery systems with high energy density. Multivalent rechargeable batteries have a theoretical high energy density that is superior to the alkaline battery system. Rechargeable magnesium-ion batteries have particular advantages such as high volumetric capacity, low reduction potential, inexpensive material costs and the dendrite-free metallic Mg anode. However, unlike the huge success of lithium-based energy storage devices in the commercial market, the development of RMBs is still in its early stage and faces many challenges in practical applications.

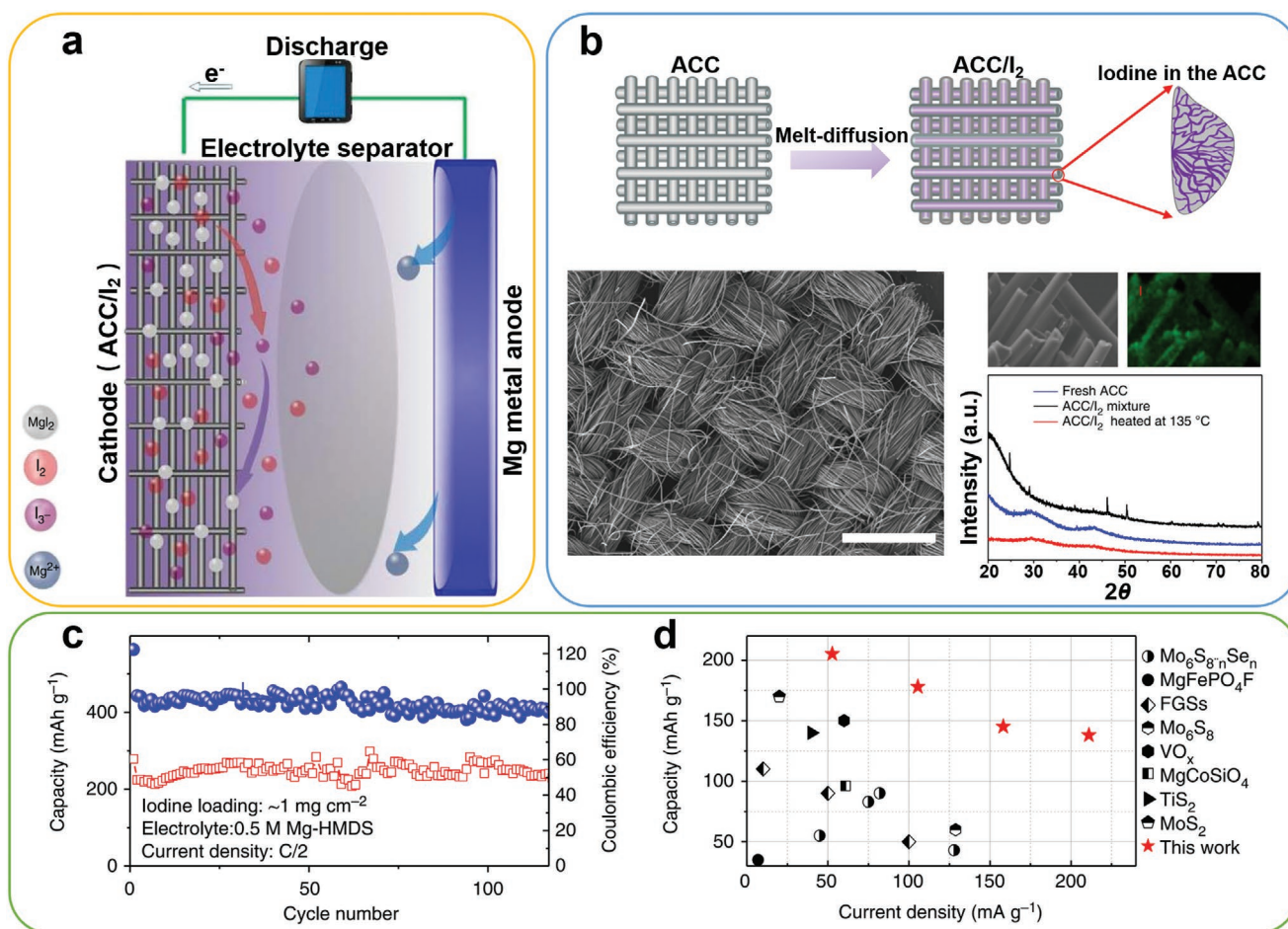


**Figure 9.** a) Schematic of rechargeable Mg-iodine batteries. b) Synthesis procedure, SEM image and energy-dispersive spectroscopy mapping of the ACC/ $I_2$  electrode. c) Cycling stability of the Mg-iodine battery at 0.5 C in 0.5 M Mg-HMDS electrolyte. d) Rate capability of the ACC/ $I_2$  electrode in comparison with other works. Reproduced with permission.<sup>[156]</sup> Copyright 2017, Nature Publishing Group.

Reasons for the patchy research progress to date are: a) the complex reaction mechanism and sluggish kinetics of Mg-based electrochemistry. The continuous deposition of Mg<sup>2+</sup> normally causes the formation of the insulated surface layer on the Mg anode in most electrolytes, which kinetically blocks relevant electrochemical reactions and the diffusion channel for Mg<sup>2+</sup> at room temperature. b) The lack of suitable cathode materials for rapid and efficient Mg<sup>2+</sup> intercalation/deintercalation at room temperature. The divalent nature and strong electrostatic interaction of Mg<sup>2+</sup> inevitably lead to sluggish kinetics. Therefore, Mg cathode materials are expected to suffer from serious structural degradation. c) The incompatibility between electrodes and electrolytes. Conventional electrolytes and nonaqueous solvents have been proven to be unsuitable for RMBs because of the formation of a nonconductive SEI layer. Moreover, most of the currently used electrolytes are air-sensitive, highly corrosive and flammable. Herein, in this progress report, we have discussed the background information, reaction mechanisms, and working principles of RMBs. The intercalation-type RMBs compounds, which are the most important and widely discussed cathode materials in RMBs system, include Chevrel phase (CP), spinel structure, layered structure, olivine structure, and NASICON structure materials. Meanwhile, cathode materials experiencing a series of conversion reactions that can achieve high theoretical capacity and energy density were also discussed. Subsequently, anode materials (apart from the commonly used Mg metal) were discussed in detail. Furthermore, other Mg-based energy storage technologies, including Mg-air, Mg-sulfur, and Mg-iodine batteries systems, have been summarized. The future development of RMBs should mainly focus on two aspects. One is the compatibility of electrode and electrolyte at room temperature. The other is the improvement of reaction kinetics and thermodynamics of RMB cathode materials. We aim to provide a comprehensive understanding of Mg-based energy storage technology, but also highlight the key points for practical applications. The multivalent rechargeable batteries could enable the development of new energy storage systems with high energy density.

## Acknowledgements

This original research was supported by the Australia Research Council, University of Technology Sydney (UTS), through the Discovery Early Career Researcher Award (DECRA DE170101009), ARC Discovery Project (DP170100436), UTS Chancellor's Postdoctoral Research Fellowship project (PRO16-1893), and UTS Early Career Researcher Grants ECRGS PRO16-1304.

## Conflict of Interest

The authors declare no conflict of interest.

## Keywords

cathode materials, diffusion, energy storage, magnesium-based batteries, reaction mechanisms

Received: November 1, 2019

Revised: March 22, 2020

Published online:

- [1] N. Kittner, F. Lill, D. M. Kammen, *Nat. Energy* **2017**, 2, 17125.
- [2] J. B. Goodenough, K.-S. Park, *J. Am. Chem. Soc.* **2013**, 135, 1167.
- [3] B. Obama, *Science* **2017**, 355, 126.
- [4] P. Poizot, S. Laruelle, S. Grugeon, L. Dupont, J. Tarascon, *Nature* **2000**, 407, 496.
- [5] B. Scrosati, J. Hassoun, Y.-K. Sun, *Energy Environ. Sci.* **2011**, 4, 3287.
- [6] V. Etacheri, R. Marom, R. Elazari, G. Salitra, D. Aurbach, *Energy Environ. Sci.* **2011**, 4, 3243.
- [7] H. D. Yoo, E. Markevich, G. Salitra, D. Sharon, D. Aurbach, *Mater. Today* **2014**, 17, 110.
- [8] A. Manthiram, *MRS Bull.* **2016**, 41, 624.
- [9] Y. Liang, Z. Chen, Y. Jing, Y. Rong, A. Facchetti, Y. Yao, *J. Am. Chem. Soc.* **2015**, 137, 4956.
- [10] J. W. Choi, D. Aurbach, *Nat. Rev. Mater.* **2016**, 1, 16013.
- [11] P. Canepa, G. Sai Gautam, D. C. Hannah, R. Malik, M. Liu, K. G. Gallagher, K. A. Persson, G. Ceder, *Chem. Rev.* **2017**, 117, 4287.
- [12] D. Aurbach, *J. Power Sources* **2000**, 89, 206.
- [13] R. Y. Wang, B. Shyam, K. H. Stone, J. N. Weker, M. Pasta, H. W. Lee, M. F. Toney, Y. Cui, *Adv. Energy Mater.* **2015**, 5, 1401869.
- [14] D. Aurbach, Z. Lu, A. Schechter, Y. Gofer, H. Gizbar, R. Turgeman, Y. Cohen, M. Moshkovich, E. Levi, *Nature* **2000**, 407, 724.
- [15] J. O. Besenhard, M. Winter, *ChemPhysChem* **2002**, 3, 155.
- [16] M. Mao, T. Gao, S. Hou, C. Wang, *Chem. Soc. Rev.* **2018**, 47, 8804.
- [17] P. Novák, R. Imhof, O. Haas, *Electrochim. Acta* **1999**, 45, 351.
- [18] J. Muldoon, C. B. Bucur, T. Gregory, *Chem. Rev.* **2014**, 114, 11683.
- [19] H. D. Yoo, I. Shterenberg, Y. Gofer, G. Gershinsky, N. Pour, D. Aurbach, *Energy Environ. Sci.* **2013**, 6, 2265.
- [20] M. Matsui, *J. Power Sources* **2011**, 196, 7048.
- [21] R. Attias, M. Salama, B. Hirsch, Y. Goffer, D. Aurbach, *Joule* **2019**, 3, 27.
- [22] J. Muldoon, C. B. Bucur, A. G. Oliver, T. Sugimoto, M. Matsui, H. S. Kim, G. D. Allred, J. Zajicek, Y. Kotani, *Energy Environ. Sci.* **2012**, 5, 5941.
- [23] S.-B. Son, T. Gao, S. P. Harvey, K. X. Steirer, A. Stokes, A. Norman, C. Wang, A. Cresce, K. Xu, C. Ban, *Nat. Chem.* **2018**, 10, 532.
- [24] Z. Lu, A. Schechter, M. Moshkovich, D. Aurbach, *J. Electroanal. Chem.* **1999**, 466, 203.
- [25] Y. Cheng, H. J. Chang, H. Dong, D. Choi, V. L. Sprenkle, J. Liu, Y. Yao, G. Li, *J. Mater. Res.* **2016**, 31, 3125.
- [26] Z. Zhao-Karger, M. Fichtner, *Front. Chem.* **2018**, 6, 656.
- [27] P. Saha, M. K. Datta, O. I. Velikokhatnyi, A. Manivannan, D. Alman, P. N. Kumta, *Prog. Mater. Sci.* **2014**, 66, 1.
- [28] I. Shterenberg, M. Salama, Y. Gofer, E. Levi, D. Aurbach, *MRS Bull.* **2014**, 39, 453.
- [29] Z. A. Zafar, S. Imtiaz, R. Razaq, S. Ji, T. Huang, Z. Zhang, Y. Huang, J. A. Anderson, *J. Mater. Chem. A* **2017**, 5, 5646.
- [30] G. A. Elia, K. Marquardt, K. Hoepfner, S. Fantini, R. Lin, E. Knipping, W. Peters, J. F. Drillet, S. Passerini, R. Hahn, *Adv. Mater.* **2016**, 28, 7564.
- [31] J. Y. Hwang, S. T. Myung, Y. K. Sun, *Adv. Funct. Mater.* **2018**, 28, 1802938.
- [32] M. Song, H. Tan, D. Chao, H. J. Fan, *Adv. Funct. Mater.* **2018**, 28, 1802564.
- [33] T. Koketsu, J. Ma, B. J. Morgan, M. Body, C. Legein, W. Dachraoui, M. Giannini, A. Demortière, M. Salanne, F. Dardoize, *Nat. Mater.* **2017**, 16, 1142.
- [34] H. D. Yoo, Y. Liang, H. Dong, J. Lin, H. Wang, Y. Liu, L. Ma, T. Wu, Y. Li, Q. Ru, *Nat. Commun.* **2017**, 8, 339.
- [35] Z. Li, X. Mu, Z. Zhao-Karger, T. Diemant, R. J. Behm, C. Kübel, M. Fichtner, *Nat. Commun.* **2018**, 9, 5115.
- [36] Z. Rong, R. Malik, P. Canepa, G. Sai Gautam, M. Liu, A. Jain, K. Persson, G. Ceder, *Chem. Mater.* **2015**, 27, 6016.

- [37] M. Liu, A. Jain, Z. Rong, X. Qu, P. Canepa, R. Malik, G. Ceder, K. A. Persson, *Energy Environ. Sci.* **2016**, *9*, 3201.
- [38] M. Liu, Z. Rong, R. Malik, P. Canepa, A. Jain, G. Ceder, K. A. Persson, *Energy Environ. Sci.* **2015**, *8*, 964.
- [39] R. Malik, D. Burch, M. Bazant, G. Ceder, *Nano Lett.* **2010**, *10*, 4123.
- [40] H. Gwon, S.-W. Kim, Y.-U. Park, J. Hong, G. Ceder, S. Jeon, K. Kang, *Inorg. Chem.* **2014**, *53*, 8083.
- [41] R. Mohtadi, M. Matsui, T. S. Arthur, S. J. Hwang, *Angew. Chem., Int. Ed.* **2012**, *51*, 9780.
- [42] Y. Shao, T. Liu, G. Li, M. Gu, Z. Nie, M. Engelhard, J. Xiao, D. Lv, C. Wang, J.-G. Zhang, *Sci. Rep.* **2013**, *3*, 3130.
- [43] J. Zhu, Y. Guo, J. Yang, Y. Nuli, F. Zhang, J. Wang, S.-i. Hirano, *J. Power Sources* **2014**, *248*, 690.
- [44] E. Guyot, S. Seghir, J. Lecuire, C. Boulanger, M. Levi, Y. Shilina, V. Dargel, D. Aurbach, *J. Electrochem. Soc.* **2013**, *160*, A420.
- [45] L. F. Wan, B. R. Perdue, C. A. Applett, D. Prendergast, *Chem. Mater.* **2015**, *27*, 5932.
- [46] D. Aurbach, G. S. Suresh, E. Levi, A. Mitelman, O. Mizrahi, O. Chusid, M. Brunelli, *Adv. Mater.* **2007**, *19*, 4260.
- [47] O. Chusid, Y. Gofer, H. Gizbar, Y. Vestfrid, E. Levi, D. Aurbach, I. Riech, *Adv. Mater.* **2003**, *15*, 627.
- [48] D. Aurbach, I. Weissman, Y. Gofer, E. Levi, *Chem. Rec.* **2003**, *3*, 61.
- [49] C. Ling, K. Suto, *Chem. Mater.* **2017**, *29*, 3731.
- [50] E. Levi, E. Lancry, A. Mitelman, D. Aurbach, G. Ceder, D. Morgan, O. Isnard, *Chem. Mater.* **2006**, *18*, 5492.
- [51] M. Levi, E. Lancry, H. Gizbar, Z. Lu, E. Levi, Y. Gofer, D. Aurbach, *J. Electrochem. Soc.* **2004**, *151*, A1044.
- [52] G. Suresh, M. Levi, D. Aurbach, *Electrochim. Acta* **2008**, *53*, 3889.
- [53] P. Xiong, R. Ma, G. Wang, T. Sasaki, *Energy Storage Mater.* **2019**, *19*, 281.
- [54] X. Zhang, L. Hou, A. Ciesielski, P. Samorì, *Adv. Energy Mater.* **2016**, *6*, 1600671.
- [55] A. Moretti, S. Passerini, *Adv. Energy Mater.* **2016**, *6*, 1600868.
- [56] E. Levi, Y. Gofer, D. Aurbach, *Chem. Mater.* **2010**, *22*, 860.
- [57] D. Imamura, M. Miyayama, M. Hibino, T. Kudo, *J. Electrochem. Soc.* **2003**, *150*, A753.
- [58] C. Drosos, C. Jia, S. Mathew, R. G. Palgrave, B. Moss, A. Kafizas, D. Vernardou, *J. Power Sources* **2018**, *384*, 355.
- [59] Y. Cheng, Y. Shao, V. Raju, X. Ji, B. L. Mehdi, K. S. Han, M. H. Engelhard, G. Li, N. D. Browning, K. T. Mueller, J. Liu, *Adv. Funct. Mater.* **2016**, *26*, 3446.
- [60] J. L. Andrews, A. Mukherjee, H. D. Yoo, A. Parija, P. M. Marley, S. Fakra, D. Prendergast, J. Cabana, R. F. Klie, S. Banerjee, *Chem* **2018**, *4*, 564.
- [61] M. Spahr, P. Novak, O. Haas, R. Nesper, *J. Power Sources* **1995**, *54*, 346.
- [62] G. Gershinsky, H. D. Yoo, Y. Gofer, D. Aurbach, *Langmuir* **2013**, *29*, 10964.
- [63] J. T. Incorvati, L. F. Wan, B. Key, D. Zhou, C. Liao, L. Fuoco, M. Holland, H. Wang, D. Prendergast, K. R. Poeppelmeier, *Chem. Mater.* **2016**, *28*, 17.
- [64] W. Kaveevivitchai, A. J. Jacobson, *Chem. Mater.* **2016**, *28*, 4593.
- [65] K. W. Nam, S. Kim, S. Lee, M. Salama, I. Shterenberg, Y. Gofer, J.-S. Kim, E. Yang, C. S. Park, J.-S. Kim, *Nano Lett.* **2015**, *15*, 4071.
- [66] D. S. Tchitchevko, A. Ponrouch, R. Verreli, T. Broux, C. Frontera, A. Sorrentino, F. Bardé, N. Biskup, M. E. Arroyo-de Domípablo, M. R. Palacín, *Chem. Mater.* **2018**, *30*, 847.
- [67] A. Emly, A. Van der Ven, *Inorg. Chem.* **2015**, *54*, 4394.
- [68] X. Sun, P. Bonnick, L. F. Nazar, *ACS Energy Lett.* **2016**, *1*, 297.
- [69] Z.-L. Tao, L.-N. Xu, X.-L. Gou, J. Chen, H.-T. Yuan, *Chem. Commun.* **2004**, 2080.
- [70] R. Ganatra, Q. Zhang, *ACS Nano* **2014**, *8*, 4074.
- [71] G. Zhang, H. Liu, J. Qu, J. Li, *Energy Environ. Sci.* **2016**, *9*, 1190.
- [72] Y. Liang, R. Feng, S. Yang, H. Ma, J. Liang, J. Chen, *Adv. Mater.* **2011**, *23*, 640.
- [73] Y. Liu, L. Jiao, Q. Wu, J. Du, Y. Zhao, Y. Si, Y. Wang, H. Yuan, *J. Mater. Chem. A* **2013**, *1*, 5822.
- [74] Y. Gu, Y. Katsura, T. Yoshino, H. Takagi, K. Taniguchi, *Sci. Rep.* **2015**, *5*, 12486.
- [75] B. Liu, T. Luo, G. Mu, X. Wang, D. Chen, G. Shen, *ACS Nano* **2013**, *7*, 8051.
- [76] M. Xu, S. Lei, J. Qi, Q. Dou, L. Liu, Y. Lu, Q. Huang, S. Shi, X. Yan, *ACS Nano* **2018**, *12*, 3733.
- [77] M.-Q. Zhao, C. E. Ren, M. Alhabeb, B. Anasori, M. W. Barsoum, Y. Gogotsi, *ACS Appl. Energy Mater.* **2019**, *2*, 1572.
- [78] F. Liu, Y. Liu, X. Zhao, X. Liu, L.-Z. Fan, *J. Mater. Chem. A* **2019**, *7*, 16712.
- [79] M. Xu, N. Bai, H.-X. Li, C. Hu, J. Qi, X.-B. Yan, *Chin. Chem. Lett.* **2018**, *29*, 1313.
- [80] Y. Li, D. Xu, D. Zhang, Y. Wei, R. Zhang, Y. Guo, *RSC Adv.* **2019**, *9*, 33572.
- [81] N. N. Sinha, N. Munichandraiah, *Electrochem. Solid-State Lett.* **2008**, *11*, F23.
- [82] C. Yuan, Y. Zhang, Y. Pan, X. Liu, G. Wang, D. Cao, *Electrochim. Acta* **2014**, *116*, 404.
- [83] M. Cabello, R. Alcantara, F. Nacimiento, G. Ortiz, P. Lavela, J. Tirado, *CrystEngComm* **2015**, *17*, 8728.
- [84] G. Liu, Q. Chi, Y. Zhang, Q. Chen, C. Zhang, K. Zhu, D. Cao, *Chem. Commun.* **2018**, *54*, 9474.
- [85] Q. D. Truong, M. Kempala Devaraju, P. D. Tran, Y. Gambe, K. Nayuki, Y. Sasaki, I. Honma, *Chem. Mater.* **2017**, *29*, 6245.
- [86] X. Sun, P. Bonnick, V. Duffort, M. Liu, Z. Rong, K. A. Persson, G. Ceder, L. F. Nazar, *Energy Environ. Sci.* **2016**, *9*, 2273.
- [87] S. K. Kolli, A. Van der Ven, *Chem. Mater.* **2018**, *30*, 2436.
- [88] A. Wustrow, B. Key, P. J. Phillips, N. Sa, A. S. Lipton, R. F. Klie, J. T. Vaughn, K. R. Poeppelmeier, *Inorg. Chem.* **2018**, *57*, 8634.
- [89] A. K. Padhi, K. S. Nanjundaswamy, J. B. Goodenough, *J. Electrochem. Soc.* **1997**, *144*, 1188.
- [90] Z. Gong, Y. Yang, *Energy Environ. Sci.* **2011**, *4*, 3223.
- [91] H. Kim, I. Park, D.-H. Seo, S. Lee, S.-W. Kim, W. J. Kwon, Y.-U. Park, C. S. Kim, S. Jeon, K. Kang, *J. Am. Chem. Soc.* **2012**, *134*, 10369.
- [92] Z. Li, L. Han, Y. Wang, X. Li, J. Lu, X. Hu, *Small* **2019**, *15*, 1900105.
- [93] A. Padhi, K. Nanjundaswamy, C. Masquelier, S. Okada, J. B. Goodenough, *J. Electrochem. Soc.* **1997**, *144*, 1609.
- [94] Y. Orikasa, T. Masese, Y. Koyama, T. Mori, M. Hattori, K. Yamamoto, T. Okado, Z.-D. Huang, T. Minato, C. Tassel, *Sci. Rep.* **2015**, *4*, 5622.
- [95] J. Heath, H. Chen, M. S. Islam, *J. Mater. Chem. A* **2017**, *5*, 13161.
- [96] T. Mori, T. Masese, Y. Orikasa, Z.-D. Huang, T. Okado, J. Kim, Y. Uchimoto, *Phys. Chem. Chem. Phys.* **2016**, *18*, 13524.
- [97] Q. D. Truong, M. K. Devaraju, I. Honma, *J. Power Sources* **2017**, *361*, 195.
- [98] Y. Zheng, Y. NuLi, Q. Chen, Y. Wang, J. Yang, J. Wang, *Electrochim. Acta* **2012**, *66*, 75.
- [99] Y. NuLi, Y. Zheng, Y. Wang, J. Yang, J. Wang, *J. Mater. Chem.* **2011**, *21*, 12437.
- [100] N. Anantharamulu, K. K. Rao, G. Rambabu, B. V. Kumar, V. Radha, M. Vithal, *J. Mater. Sci.* **2011**, *46*, 2821.
- [101] S. P. Ong, V. L. Chevrier, G. Hautier, A. Jain, C. Moore, S. Kim, X. Ma, G. Ceder, *Energy Environ. Sci.* **2011**, *4*, 3680.
- [102] J. Kang, H. Chung, C. Doh, B. Kang, B. Han, *J. Power Sources* **2015**, *293*, 11.
- [103] S.-C. Yin, H. Grondy, P. Strobel, M. Anne, L. F. Nazar, *J. Am. Chem. Soc.* **2003**, *125*, 10402.
- [104] K. Makino, Y. Katayama, T. Miura, T. Kishi, *J. Power Sources* **2001**, *99*, 66.

- [105] K. Makino, Y. Katayama, T. Miura, T. Kishi, *J. Power Sources* **2001**, 97–98, 512.
- [106] K. Makino, Y. Katayama, T. Miura, T. Kishi, *J. Power Sources* **2002**, 112, 85.
- [107] Z.-D. Huang, T. Masese, Y. Orikasa, T. Mori, *RSC Adv.* **2015**, 5, 8598.
- [108] F. Wu, G. Yushin, *Energy Environ. Sci.* **2017**, 10, 435.
- [109] S. H. Yu, S. H. Lee, D. J. Lee, Y. E. Sung, T. Hyeon, *Small* **2016**, 12, 2146.
- [110] D. A. Kitchaev, S. T. Dacek, W. Sun, G. Ceder, *J. Am. Chem. Soc.* **2017**, 139, 2672.
- [111] B. Li, G. Rong, Y. Xie, L. Huang, C. Feng, *Inorg. Chem.* **2006**, 45, 6404.
- [112] D. Su, H.-J. Ahn, G. Wang, *J. Mater. Chem. A* **2013**, 1, 4845.
- [113] S. Zhao, T. Liu, D. Shi, Y. Zhang, W. Zeng, T. Li, B. Miao, *Appl. Surf. Sci.* **2015**, 351, 862.
- [114] C. Ling, R. Zhang, T. S. Arthur, F. Mizuno, *Chem. Mater.* **2015**, 27, 5799.
- [115] R. Zhang, T. S. Arthur, C. Ling, F. Mizuno, *J. Power Sources* **2015**, 282, 630.
- [116] R. Zhang, X. Yu, K.-W. Nam, C. Ling, T. S. Arthur, W. Song, A. M. Knapp, S. N. Ehrlich, X.-Q. Yang, M. Matsui, *Electrochem. Commun.* **2012**, 23, 110.
- [117] X. Sun, V. Duffort, B. L. Mehdi, N. D. Browning, L. F. Nazar, *Chem. Mater.* **2016**, 28, 534.
- [118] S. Zhao, T. Liu, D. Hou, W. Zeng, B. Miao, S. Hussain, X. Peng, M. S. Javed, *Appl. Surf. Sci.* **2015**, 356, 259.
- [119] M. Wu, Y. Zhang, T. Li, Z. Chen, *Nanoscale* **2018**, 10, 12526.
- [120] Z. Wang, S. Rafai, C. Qiao, J. Jia, Y. Zhu, X. Ma, C. Cao, *ACS Appl. Mater. Interfaces* **2019**, 11, 7046.
- [121] F. Xiong, Y. Fan, S. Tan, L. Zhou, Y. Xu, C. Pei, Q. An, L. Mai, *Nano Energy* **2018**, 47, 210.
- [122] J. Song, E. Sahadeo, M. Noked, S. B. Lee, *J. Phys. Chem. Lett.* **2016**, 7, 1736.
- [123] Y.-H. Tan, W.-T. Yao, T. Zhang, T. Ma, L.-L. Lu, F. Zhou, H.-B. Yao, S.-H. Yu, *ACS Nano* **2018**, 12, 5856.
- [124] D. J. Wetzel, M. A. Malone, R. T. Haasch, Y. Meng, H. Vieker, N. T. Hahn, A. Gölzhäuser, J.-M. Zuo, K. R. Zavadil, A. A. Gewirth, *ACS Appl. Mater. Interfaces* **2015**, 7, 18406.
- [125] N. Wu, Y.-C. Lyu, R.-J. Xiao, X. Yu, Y.-X. Yin, X.-Q. Yang, H. Li, L. Gu, Y.-G. Guo, *NPG Asia Mater.* **2014**, 6, e120.
- [126] J. Zeng, Y. Yang, C. Li, J. Li, J. Huang, J. Wang, J. Zhao, *Electrochim. Acta* **2017**, 247, 265.
- [127] Y. Meng, D. Wang, Y. Zhao, R. Lian, Y. Wei, X. Bian, Y. Gao, F. Du, B. Liu, G. Chen, *Nanoscale* **2017**, 9, 12934.
- [128] N. Singh, T. S. Arthur, C. Ling, M. Matsui, F. Mizuno, *Chem. Commun.* **2013**, 49, 149.
- [129] L. R. Parent, Y. Cheng, P. V. Sushko, Y. Shao, J. Liu, C.-M. Wang, N. D. Browning, *Nano Lett.* **2015**, 15, 1177.
- [130] Y. Shao, M. Gu, X. Li, Z. Nie, P. Zuo, G. Li, T. Liu, J. Xiao, Y. Cheng, C. Wang, *Nano Lett.* **2014**, 14, 255.
- [131] J. Niu, H. Gao, W. Ma, F. Luo, K. Yin, Z. Peng, Z. Zhang, *Energy Storage Mater.* **2018**, 14, 351.
- [132] J. Zhang, B. Sun, Y. Zhao, A. Tkacheva, Z. Liu, K. Yan, X. Guo, A. M. McDonagh, D. Shanmukaraj, C. Wang, *Nat. Commun.* **2019**, 10, 602.
- [133] L. Ma, S. Chen, Z. Pei, Y. Huang, G. Liang, F. Mo, Q. Yang, J. Su, Y. Gao, J. A. Zapien, *ACS Nano* **2018**, 12, 1949.
- [134] J. S. Lee, S. Tai Kim, R. Cao, N. S. Choi, M. Liu, K. T. Lee, J. Cho, *Adv. Energy Mater.* **2011**, 1, 34.
- [135] T. Zhang, Z. Tao, J. Chen, *Mater. Horiz.* **2014**, 1, 196.
- [136] G. Hoey, M. Cohen, *J. Electrochem. Soc.* **1958**, 105, 245.
- [137] W.-K. Hu, D. Noréus, *J. Power Sources* **2010**, 195, 5810.
- [138] Y. Feng, W. Xiong, J. Zhang, R. Wang, N. Wang, *J. Mater. Chem. A* **2016**, 4, 8658.
- [139] F. W. Richey, B. D. McCloskey, A. C. Luntz, *J. Electrochem. Soc.* **2016**, 163, A958.
- [140] C. S. Li, Y. Sun, F. Gebert, S. L. Chou, *Adv. Energy Mater.* **2017**, 7, 1700869.
- [141] T. Shiga, Y. Hase, Y. Kato, M. Inoue, K. Takechi, *Chem. Commun.* **2013**, 49, 9152.
- [142] C.-S. Li, Y. Sun, W.-H. Lai, J.-Z. Wang, S.-L. Chou, *ACS Appl. Mater. Interfaces* **2016**, 8, 27710.
- [143] B. Sievert, J. Häcker, F. Bienen, N. Wagner, K. A. Friedrich, *ECS Trans.* **2017**, 77, 413.
- [144] Y. Chen, W. Zhang, D. Zhou, H. Tian, D. Su, C. Wang, D. Stockdale, F. Kang, B. Li, G. Wang, *ACS Nano* **2019**, 13, 4731.
- [145] J. Xu, W. Zhang, Y. Chen, H. Fan, D. Su, G. Wang, *J. Mater. Chem. A* **2018**, 6, 2797.
- [146] Y. Chen, S. Choi, D. Su, X. Gao, G. Wang, *Nano Energy* **2018**, 47, 331.
- [147] Y. Xu, Y. Ye, S. Zhao, J. Feng, J. Li, H. Chen, A. Yang, F. Shi, L. Jia, Y. Wu, *Nano Lett.* **2019**, 19, 2928.
- [148] B. Vinayan, Z. Zhao-Karger, T. Diemant, V. S. K. Chakravadhanula, N. I. Schwarzburger, M. A. Cambaz, R. J. Behm, C. Kübel, M. Fichtner, *Nanoscale* **2016**, 8, 3296.
- [149] X. Zhou, J. Tian, J. Hu, C. Li, *Adv. Mater.* **2018**, 30, 1704166.
- [150] Z. Meng, D. Foix, N. Brun, R. Dedryvère, L. Stievano, M. Morcrette, R. Berthelot, *ACS Energy Lett.* **2019**, 4, 2040.
- [151] H. S. Kim, T. S. Arthur, G. D. Allred, J. Zajicek, J. G. Newman, A. E. Rodnyansky, A. G. Oliver, W. C. Boggess, J. Muldoon, *Nat. Commun.* **2011**, 2, 427.
- [152] Z. Zhao-Karger, X. Zhao, D. Wang, T. Diemant, R. J. Behm, M. Fichtner, *Adv. Energy Mater.* **2015**, 5, 1401155.
- [153] Z. Zhao-Karger, R. Liu, W. Dai, Z. Li, T. Diemant, B. Vinayan, C. Bonatto Minella, X. Yu, A. Manthiram, R. J. r. Behm, *ACS Energy Lett.* **2018**, 3, 2005.
- [154] A. Du, Z. Zhang, H. Qu, Z. Cui, L. Qiao, L. Wang, J. Chai, T. Lu, S. Dong, T. Dong, *Energy Environ. Sci.* **2017**, 10, 2616.
- [155] T. Gao, S. Hou, F. Wang, Z. Ma, X. Li, K. Xu, C. Wang, *Angew. Chem.* **2017**, 129, 13711.
- [156] H. Tian, T. Gao, X. Li, X. Wang, C. Luo, X. Fan, C. Yang, L. Suo, Z. Ma, W. Han, *Nat. Commun.* **2017**, 8, 14083.